The ^{60}Co Calibration of the ZEUS Calorimeters

by

Ling-Wai Hung
Department of Physics, McGill University
Montréal, Québec
July 1991

A Thesis submitted to the
Faculty of Graduate Studies and Research
in partial fulfillment of the requirements for the degree of
Master of Science

© Ling-Wai Hung, 1991

Abstract

The calibration and quality control measurements of the ZEUS forward and rear calorimeters made using movable ^{60}Co sources are described. The types of assembly faults discovered from the runs taken first at CERN and then later at DESY from mid 1990 to early 1991 are presented. The WLS attenuation length as well as changes in the attenuation length of the scintillators can be monitored by the cobalt scans.

Résumé

Le processus de calibration et de mise au point des calorimetres avant et arrière du détecteur ZEUS en utilisant une source mobile de ^{60}Co est decrit en detail. Les différentes erreurs d'assemblage découvertes lors des expériences au CERN puis à DESY au cours des années 1990 et 1991 sont également présentées. L'atténuation des dephaseurs et les changements de la longueur d'atténuation des scintillateurs peuvent être estimés en utilisant une source de ^{60}Co.

Contents

List of Figures

List of Tables

My work would not be possible without the contributions by the members of the ZEUS collaboration who designed, built and prepared the ZEUS calorimeter. I would like to thank them for allowing me to participate in such a worthwhile project. I would also like to thank my supervisor David Hanna for all the advice and motivation which he provided.

Life in Germany would not have been the same without the support of the fellow Canadian students, post-docs and professors working at DESY who were always willing to help or offer advice. Among them, I would like to particularly thank Dave Gilkinson who did much of the building and programming of the source driver, most of the inside scanning and, perhaps more importantly, introduced me to nightlife in Hamburg.

I would like to give very special thanks my German colleagues, Gerrit Gloth, Bodo Krebs and Focko Meyer, who constructed the outside scanner and spent with me many long days and nights scanning the modules. Gerrit and Focko showed me how to use their analysis programs as well provided me with the WLS and scintillator attenuation data. Bodo, who led our little group, did much of the visual analysis of the source plots, drew the source driver diagrams and offered many helpful suggestions.

And I must thank my friends and family for their continual support throughout this entire endeavour.

Chapter 1

Introduction

1.1 Background

Inquiring minds have often posed the questions; *Who are we?* and *What are we made of?* While philosophers are still tackling the former, modern science has made considerable progress towards answering the latter, at least in a material sense, during the past century and a half. Starting with Mendeleev, who a little over a hundred years ago organized the periodic table, our insight into the underlying structure of Nature has grown increasingly sophisticated In his time atoms were believed to be the smallest units of matter. By 1932 the discoveries of the electron, proton and neutron seemed to fully explain the structure of the periodic table and it was thought that they were the basic constituents of all things. However, later experiments using cosmic rays and accelerators revealed a rich spectrum of hadronic particles, implying the existence of a great variety of fundamental particles. In 1964 Gell-Mann and Zweig proposed that the multiplicity of hadrons could be explained by SU(3) symmetry through the introduction of even more elementary particles called quarks[1]. Today we believe that all matter is built from six quarks, six leptons and their antiparticles. They interact through the interchange of gauge bosons associated with four fundamental forces, strong, weak, electromagnetic and gravitational, which themselves may be manifestations of a single unified force. Already the weak and electromagnetic forces are known to be aspects of a single electro-weak force. All particles and three forces (gravitation excluded) are accounted for by the currently held theory called the 'standard model'. The growth of our understanding from the periodic table to the standard model can largely be attributed to the rapid succession of experiments stimulating or confirming theoretical ideas which in turn formed the bases for further experiments.

One type of such experiments which has made important contributions to the development of the standard model, and in particular to the understanding of the structure of the nucleon, is the scattering of leptons by hadrons. Since leptons are considered to be point particles, they are ideal for probing the substructure of the nucleon. Evidence for the existence of pointlike, charged 'partons' within the proton was first provided in 1968 at SLAC where electrons of energies 9-16 GeV were scattered off protons[2]. There, the scattering cross sections at high momentum transfers behaved more like the elastic scattering off point-like objects than like the inelastic breakup of the proton. These partons were eventually identified with the quarks previously postulated by Gell-Mann and Zweig to explain the hadronic spectrum. Hadrons are believed to be made of two or three valence quarks in a sea of virtual quark-antiquark pairs. The quarks carry a colour charge and interact mainly through the strong force mediated by the exchange of gluons in analogy to the electromagnetic force where the photon is the mediator.

The HERA accelerator (see Figure 1.1) at DESY in Hamburg will collide 30 GeV electrons with 820 GeV protons yielding a centre of mass (cms) energy of $\sqrt{s} \approx 314$ GeV[3]. As the world's first electron-proton collider, it will cover a range of momentum transfers (Q) reaching up to $Q^2 \sim 10^5 (GeV/c)^2$, a great increase from previous experiments using fixed targets which could only reach Q^2 of a few hundred $(GeV/c)^2$. However the interaction cross section decreases roughly as $1/Q^2$, making high luminosity a priority in order to acquire sufficient statistics in the high Q^2 region. HERA therefore has 210 bunches of both electrons and protons each containing $\mathcal{O}(10^{11})$ particles. With a bunch crossing occurring every 96 ns, a luminosity of $1.5 \cdot 10^{31}\ cm^{-2}/s$

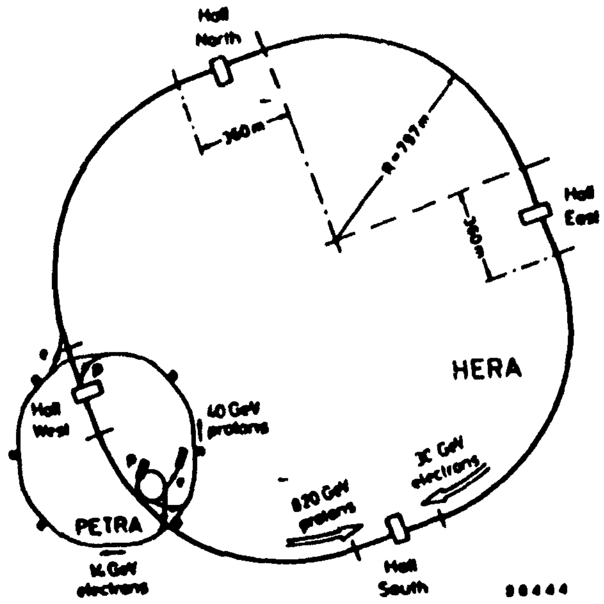

Figure 1.1: *Layout of the HERA Ring*

can be obtained (see Table 1.1). The distance scale of the interactions between leptons and quarks which is accessible by HERA is of the order 10^{-18}cm.

1.2 Kinematics

The principle processes in deep inelastic scattering at HERA energies occur through neutral current (NC) interactions exchanging a γ or Z° boson with a parton from the proton, and charged current (CC) interactions exchanging a $W^\pm$ (see Figure 1.2). In CC processes, the final state lepton is a neutrino and leaves the detector undetected. In both cases the scattered parton is seen in the detector as a 'jet' of hadronic particles emitted in a narrow cone balancing the lepton in transverse momentum. The remnants of the proton continue on and most are lost down the beam pipe.

There are only two independent variables in the overall event kinematics, both of which can be measured from either the electron or jet (using the Jacquet-Blondel

Parameter	proton ring		electron ring	units
Nominal energy	820		30	GeV
c.m. energy		314		GeV
Q^2_{max}		98400		$(GeV/c)^2$
Luminosity		$1.5 \cdot 10^{31}$		$cm^{-2}s^{-1}$
Number of interaction points		4		
Crossing angle		0		$mrad$
Circumference		6336		m
Magnetic field	4.65		0.165	T
Energy Range	300-820		10-33	GeV
Injection energy	40		14	GeV
Circulating currents	160		58	mA
Total number of particles	$2.1 \cdot 10^{13}$		$0.8 \cdot 10^{13}$	
Number of bunches		200		
Number of buckets		220		
Time between crossings		96		ns
Total RF power	1		13.2	MW
Filling time	20		15	$min.$

Table 1.1: *Parameters of the HERA collider*

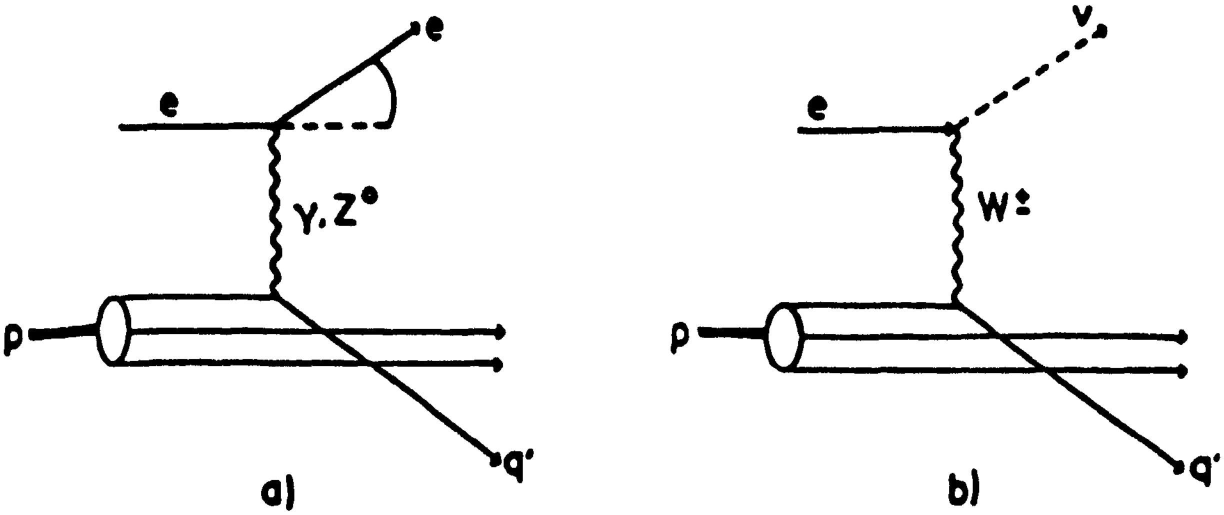

Figure 1.2: *Feynman diagrams of lowest order a) NC and b) CC interactions*

method[4]) alone. To define the kinematic relations we let p_e and p_l be the four vectors of the incoming and scattered lepton respectively, P that of the incoming proton, and $q = p_e - p_l$ that of the exchange boson.

The total invariant mass squared is

$$\begin{aligned} s &\equiv (p_e + P)^2 \\ &\approx 4E_eE_p. \end{aligned}$$

The approximation assumes the particle masses to be zero, which is very reasonable at HERA energies. The square of the four momentum transfer, Q^2, is defined to be positive

$$\begin{aligned} Q^2 &\equiv -q^2 \\ &= -(p_e - p_l)^2 \\ &\approx 4E_eE_l \sin^2\frac{\theta_l}{2}. \end{aligned}$$

The energy of the current in the target rest frame, ν is

$$\begin{aligned} \nu &\equiv \frac{P \cdot q}{m_p} \\ &\approx \frac{2E_p}{m_p}(E_e - E_l cos^2\frac{\theta_l}{2}). \end{aligned}$$

The dimensionless variables Bjorken-x and y are given by

$$\begin{aligned} x &\equiv \frac{Q^2}{2P \cdot q} \\ &= \frac{Q^2}{2m_p\nu} \\ &\approx \frac{E_eE_l \sin^2\frac{\theta l}{2}}{E_p(E_e - E_l \cos^2\frac{\theta_l}{2})} \end{aligned}$$

$$\begin{aligned} y &\equiv \frac{P \cdot q}{P \cdot p_e} \\ &= \frac{2P \cdot q}{s} \\ &= \frac{\nu}{\nu_{max}} \\ &\approx \frac{E_e - E_l \cos^2\frac{\theta_l}{2}}{E_e}. \end{aligned}$$

They are always in the range $0 \leq (x, y) \leq 1$. In the parton model, x can be identified with the momentum fraction of the proton carried by the struck parton whereas y is a measure of the inelasticity of the event. Another useful quantity, the invariant mass W of the hadronic system, is given by

$$\begin{aligned} W^2 &\equiv (q+P)^2 \\ &= Q^2\frac{1-x}{x} + {m_p}^2. \end{aligned}$$

An accurate measurement of the kinematics of an event requires a high resolution hermetic calorimeter. In the case of CC processes, one cannot measure the outgoing lepton and must instead rely on only the jet measurements for a description of the event. Even when the electron is present, as in NC processes, the electron is often in a kinematic region where a small error in the measurement of the electron's momentum means a large error in x or Q^2 (see Figure 1.3). Although tracking detectors also give momentum information, their fractional resolution, σ_p/p, grows linearly with p. In addition, they are effective only for charged particles. On the other hand, a calorimeter has a fractional resolution improving as $1/\sqrt{E}$ and is sensitive to some neutral particles as well as charged ones. Using the calorimeter for measuring the event kinematics also requires it to have fine segmentation for good angular resolution and good hadron-electron discrimination to distinguish electrons from pions.

1.3 HERA Physics

A broad range of physics prospects is available at HERA [5]. Structure functions, heavy quark physics, compositeness, low-x physics and searches for exotic particles such as leptoquarks are all potential of areas of research. In particular, the study of the evolution of the structure functions of the proton with Q^2 is of prime importance. These structure functions, which depend on the probing leptons' polarization, are related to the quark and gluon densities of the proton. The cross section for deep

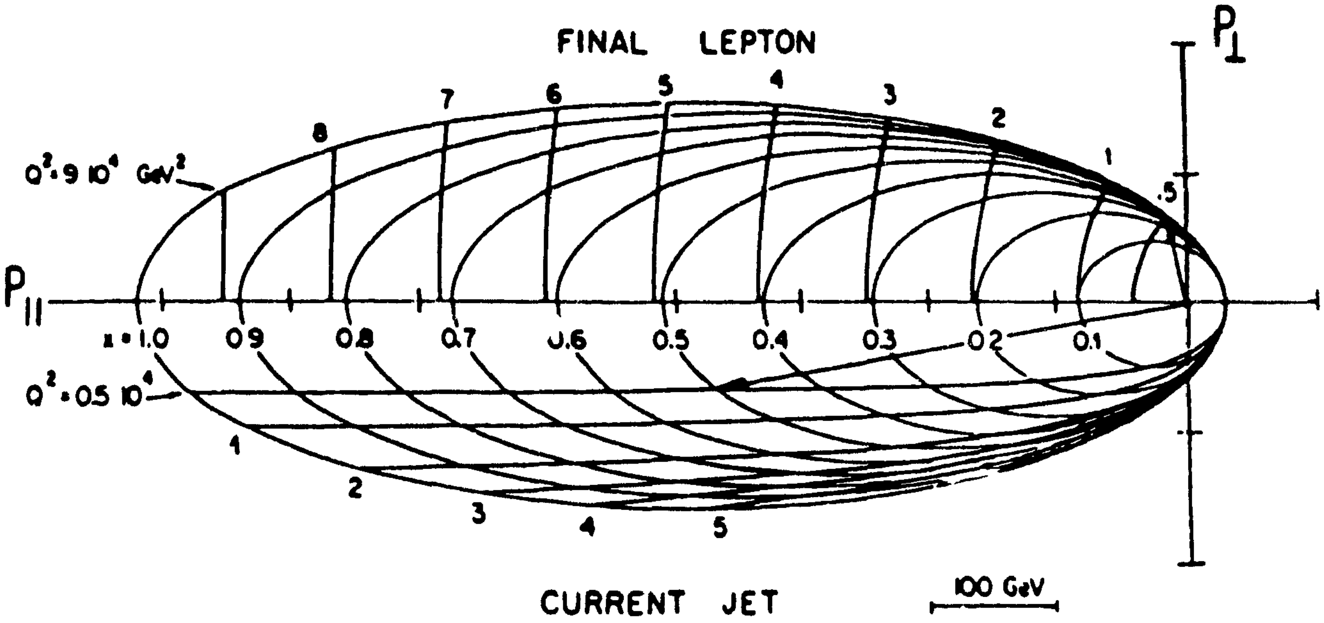

Figure 1.3: *Polar diagram of the kinematics for the final lepton (upper part) and the current jet (lower part) with lines of constant* x *and* Q^2. *Connecting a given* (x, Q^2) *point with the origin gives the laboratory momentum vectors, as shown by the example for* $x = 0.5, Q^2 = 5000 GeV^2$.

inelastic scattering is expressed in terms of the structure functions F_1, F_2 and F_3 by

$$\frac{d^2\sigma(e^-p)}{dxdQ^2} = \frac{4\pi\alpha^2 P^2(Q^2)}{x}\{y^2 xF_1(x,Q^2) + (1-y)F_2(x,Q^2) + (y - \frac{y^2}{2} xF_3(x,Q^2))\}.$$

The propagator $P(Q^2)$ is of the form $1/Q^2$ for single γ exchange, $1/(Q^2 + M_Z^2)$ for single Z^0 exchange, $1/Q^2 + M_W^2)$ for single $W^\pm$ exchange and $1/Q^2(Q^2 + M_Z^2)$ as the γ - Z interference term.

The forms of the propagators show that the pure γ exchange term completely dominates at low Q^2. HERA is however unique because it can attain high Q^2 values where the contributions from $W^\pm$, Z exchange become important.

The structure functions are predicted by QCD (quantum chromodynamics) to decrease logarithmically with increasing Q^2 due to gluon emission by the scattered quark. Precise measurements of the structure functions at HERA can provide a stringent test of QCD as well as search for new substructure in electrons or quarks.

1.4 The ZEUS Detector

The ZEUS detector, as shown in Figures 1.4 and 1.5, is one of two detectors that will investigate e-p collisions in the HERA ring[6].

Its development and construction required the combined efforts of a collaboration of 50 institutes from 10 countries including about 350 physicists. Its principle feature is a high resolution fully compensating calorimeter. The asymmetry of the HERA collisions, with the cms frame moving in the forward, or proton direction, is reflected in the design of the detector where more emphasis is placed in the forward direction. Here, an overview of the entire detector is presented.

Closest to the interaction region is a vertex detector (VXD). It uses a time expansion drift type cell to detect the decays of short lived particles. With an impact parameter resolution of ~ 50μm it can detect particles with lifetimes greater than 10^{-13} s. Next comes the central tracking detector (CTD). It is a cylindrical jet type drift chamber with an outer radius of 85 cm and a length of 240 cm. There are 9 superlayers each with 8 layers of sense wires to measure track positions and dE/dx.

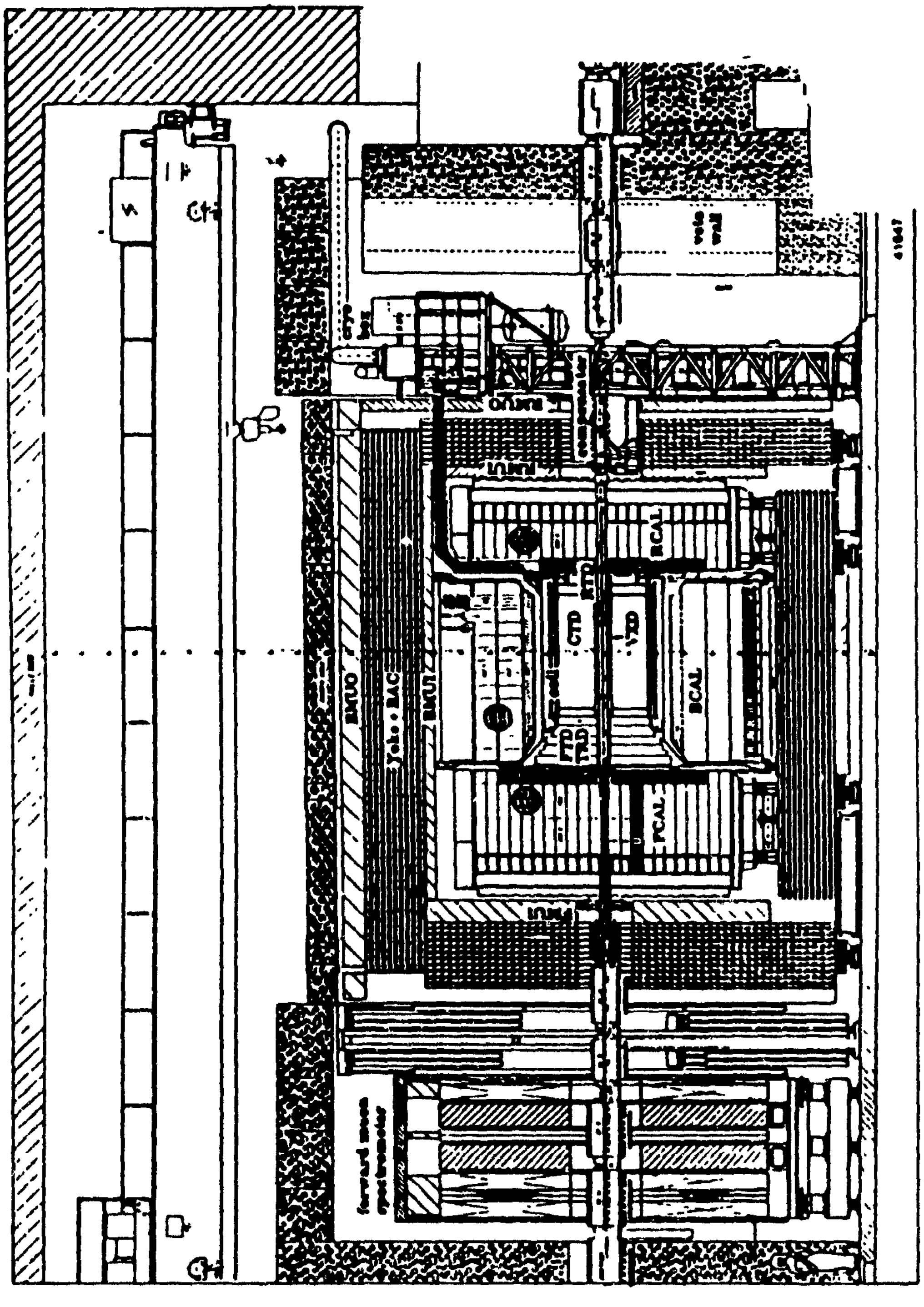

Figure 1.4: *View of the ZEUS Detector*

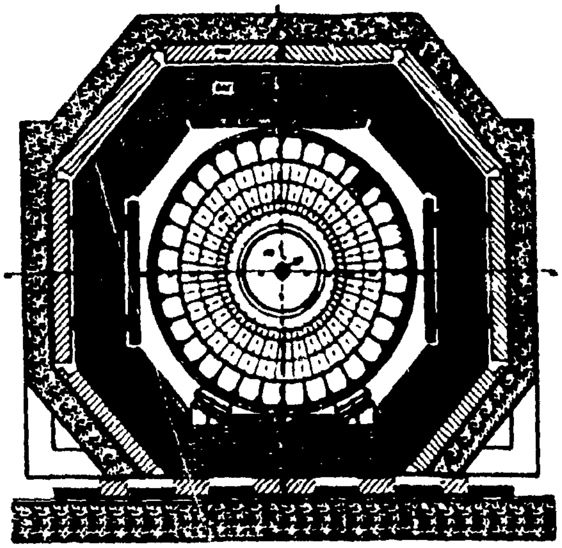

Figure 1.5: *Cross Sectional View of the ZEUS Detector*

Four of the superlayers have wires at a stereo angle of about 5 degrees in order to attain roughly equal angular resolution in the z and azimuthal directions. The precision is better than 100μm. For particles going perpendicular to the magnetic field the expected momentum resolution is

$$\frac{\sigma(p)}{p} = 0.0002 \cdot p \oplus 0.003,$$

where p is in units of GeV/c and $\oplus$ means addition in quadrature.

Complementing the CTD are forward and rear planar track detectors (FTD, RTD) consisting of three and one planar drift chambers respectively. A transition radiation detector (TRD) consisting of 4 modules sandwiched between the FTD chambers improves electron identification in the forward region. Around these inner detectors is a thin superconducting solenoid providing a magnetic field of 1.8 T.

Surrounding the entire solenoidal coil and the tracking detectors is the ZEUS calorimeter. It is a high resolution sampling calorimeter made from layers of depleted uranium (DU) plates interleaved with plastic scintillator tiles. The scintillator light from two sides of a tile is transported via wavelength shifter bars (WLS) and light guides (LG) to photomultiplier tubes (PM). Mechanically, the calorimeter is divided into three main components, the forward (FCAL), barrel (BCAL) and rear (RCAL) calorimeters, with a depth of 7, 5, 4 nuclear absorption lengths respectively to match the asymmetry of HERA's collisions. FCAL covers the polar angles from $\theta = 2.2^\circ$ to 39.9°, BCAL extends from $\theta = 36.7^\circ$ to 129.2°, and RCAL covers $\theta = 128.1^\circ$ to 176.5°. Together they cover 99.8% of the solid angle in the forward hemisphere and 99.5% in the backward hemisphere. Longitudinally they are segmented into 2 parts. The inner part, with a depth of about 25 radiation lengths X_0 ($\sim$ one nuclear absorption length, λ), is called the electromagnetic calorimeter (EMC). The remaining, outer part is called the hadronic calorimeter (HAC) which is further subdivided into two subsections (HAC1 and HAC2) in the FCAL and BCAL components. The division between the EMC and HAC sections greatly helps in distinguishing between electromagnetic showers ($e^\pm,\gamma$) and hadronic showers because incident electrons or gammas will deposit almost all their energy in the EMC section whereas hadrons will deposit a substantial fraction in the HAC sections. The EMC and HAC sections in FCAL and RCAL are nonprojective. For BCAL the EMC section is projective in both the polar angle, θ, and the azimuthal angle, ϕ. The HAC sections are projective only in ϕ. FCAL and RCAL are divided into tower cells of 20 x 20 cm^2 for readout in the HAC sections. In FCAL and RCAL the EMC towers, except for those behind BCAL (called HAC0), are further segmented into 5 x 20 cm^2 and 10 x 20 cm^2 sections respectively. To help distinguish electrons from pions, especially within jets, provisions have been made to place two layers of 3 x 3 cm^2 silicon detectors, called hadron electron separators (HES), at a depth of 3 and 6 X_0 inside the EMC section of FCAL. RCAL and BCAL have space for only one layer after 3 X_0. The small size of the HES diodes and their forward positioning allow them to differentiate between electrons and hadrons because electron showers are narrower and develop more quickly than hadron showers.

The energy resolution for the calorimeter determined from test beams is for electrons $\sigma(E)/E = 18\%/\sqrt{E} \oplus 1\%$ and for hadrons $\sigma(E)/E = 35\%/\sqrt{E} \oplus 2\%$.

The backing calorimeter (BAC) surrounds the high resolution calorimeter in order to measure the energy of late showering particles. It uses iron plates as absorber, which also form the magnet's yoke, and proportional tubes of aluminum as the signal layers. The resolution for hadrons is $\sigma(E)/E = 100\%/\sqrt{E}$ Behind the yoke are the muon detectors The barrel and rear muon detectors use limited streamer tubes to identify tracks penetrating the calorimeter. They differentiate between events arising from cosmic ray and halo muons background from those originating in the interaction region. The forward muon spectrometer (FMUON) provides an independent momentum measurement of muons as well as improves the rejection of muons from background sources. It uses a toroidally magnetised iron region interleaved with drift chambers, limited streamer tubes, and time-of-flight counters A leading proton spectrometer (LPS) tags elastically scattered protons which would otherwise escape down the beam pipe. In addition, luminosity monitors upstream (in the proton direction) from the interaction region detect photons and electrons from bremsstrahlung events as well as flag low Q^2 photoproduction events.

The detector is structurally divided such that inner components are supported by the bottom yoke and outer ones are on a retractable clam shell.

In an effort to achieve and maintain its design energy resolution, the ZEUS calorimeter was built under strict quality control and equipped with various calibration systems. This thesis deals with the description of one such system which uses movable ^{60}Co sources to scan for assembly errors as well as to monitor the long term stability of the optical readout. In the following chapters the operation and results from the ^{60}Co scans first taken during the summer of 1990 at CERN and then later at DESY from the fall of 1990 to the spring of 1991 are described. Chapter 2 gives an overview of calorimetry as well as a detailed description of the calorimeter. Chapter 3 provides details of the actual operation while scanning with ^{60}Co sources. Chapter 4 presents some results from Monte Carlo simulations of the cobalt source scans. Chapter 5 summarizes the findings from the initial cobalt scans taken before the installation of the calorimeter in the detector. Finally Chapter 6 gives some conclusions and a glance at the future applications of the cobalt calibration system.

Chapter 2

The Calorimeter

2.1 Calorimetry

A calorimeter is a device to measure the energy of a particle entering it by fully absorbing its energy and producing a measurable signal proportional to it. When a particle enters a calorimeter it will interact with the material, producing secondary particles which in turn produce more particles propagating through the calorimeter. As this continues, a particle 'shower' develops. Two types of showers can be distinguished; electromagnetic and hadronic. Electromagnetic showers are made up of gammas, electrons and positrons which interact only electromagnetically through a few well understood processes which are in principle fully described by quantum electrodynamics. In comparison, hadronic showers are much more complicated, involving strongly interacting particles undergoing nuclear processes. A great deal of effort was devoted during the mid to late eighties to understand the underlying processes occurring in hadronic showers. Through detailed Monte Carlo studies[7][8][9] simulating the development of hadronic showers, some understanding of the contributions to the measured signal from the various shower components has been achieved.

2.1.1 Sampling Calorimeters

Sampling calorimeters are composed of interleaved layers of passive absorber layers and active detector layers Because materials suited for detecting particles tend to be made from light elements, alone they would require a very large volume to stop particles. The presence of absorber layers made from high Z elements remedies this by causing a shower to develop more quickly. This allows sampling calorimeters to be compact, saving much in cost and space compared to homogeneous calorimeters. Also, by correctly selecting the materials and the thicknesses of the absorber and active layers, it is possible to obtain an equal response from the electromagnetic and hadronic components of a shower. This turns out to be a critical requirement for achieving good hadronic energy resolution.

Sampling calorimeters, however, introduce fluctuations in the energy measurement, degrading their resolution. These intrinsic sampling fluctuations occur because the shower is sampled only in the active layers; i.e. only the energy deposited in the active layers produces a measurable signal. The sampling fluctuations are mostly the fluctuations in the number of charged particles crossing the active layers. The sampling resolution, σ_{samp}, is proportional to the square root of the thickness of the sampling layers. In electromagnetic (EM) showers sampling fluctuations are the largest contributors to the energy resolution.

Also contributing to sampling fluctuations are Landau and path length fluctuations. Landau fluctuations occur because a particle can deposit, through the production of energetic delta electrons, much more energy in an active layer that the average dE/dx loss through ionization. Path length fluctuations are due to the multiple scatterings of a charged particle from Coulomb interactions with the nuclear electric field which can cause it to travel a long distance in an active layer and therefore deposit more energy in there.

Other possible contributors to the resolution are energy leakage out of the calorimeter, detector imperfections, noise, photoelectron statistics and pileup effects.

2.1.2 Electromagnetic Showers

When a photon, electron or positron enters a calorimeter it will create an electromagnetic shower. The main processes involved are the following:

- Bremsstrahlung : In the electric field of an atom a high energy electron can be deflected and emit an energetic photon. The energy loss per unit length goes as Z^2.
- Pair production : A photon with at least twice the rest energy of an electron (1.022 MeV) transforms into an electron-positron pair. This can only occur in the presence of a third body, usually a nucleus, to conserve momentum. The cross section goes as Z^2.
- Compton Scattering : The photon loses energy by the inelastic scattering off atomic electrons. The cross section is proportional to Z.
- Photoelectric effect : The photon is totally absorbed by an atomic electron, freeing it from the atom. The cross section increases as Z^4 or Z^5.
- Ionization : Charged particles ionize electrons from neighbouring atoms, producing secondary electrons and excited atoms. The energy loss per unit length goes as $Z \log Z$.

From Figures 2.1 and 2.2 we can see that an EM shower will go through two stages. In the beginning energetic particles lose energy through bremsstrahlung and pair production. This continues until the particle reaches a certain threshold energy, called the critical energy ϵ_c, at which the energy loss to bremsstrahlung is equal to the ionization loss. Afterwards, in the later stage of the shower, shower particles lose their energy through ionization before being able to produce new particles and shower multiplication stops. This ionization energy deposited by low energy particles at the end of the shower constitutes a large fraction of the measured signal. The critical

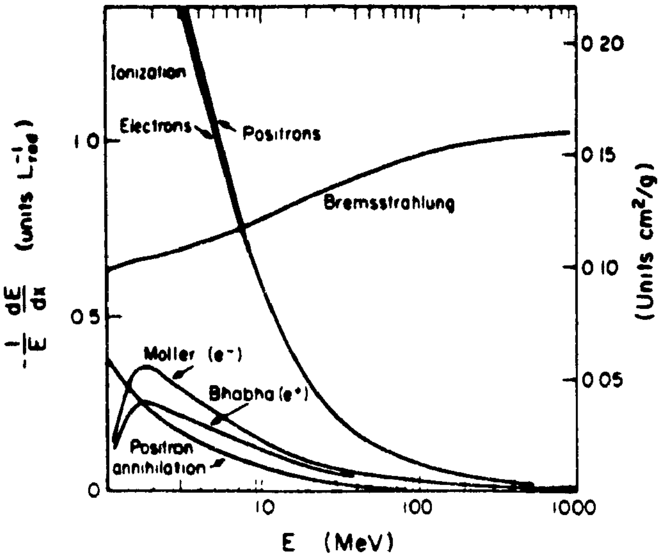

Figure 2.1: *Fractional Energy Loss for Electrons and Positrons in Lead (from Rev. of Part. Prop., Phys Let. B. Vol 239)*

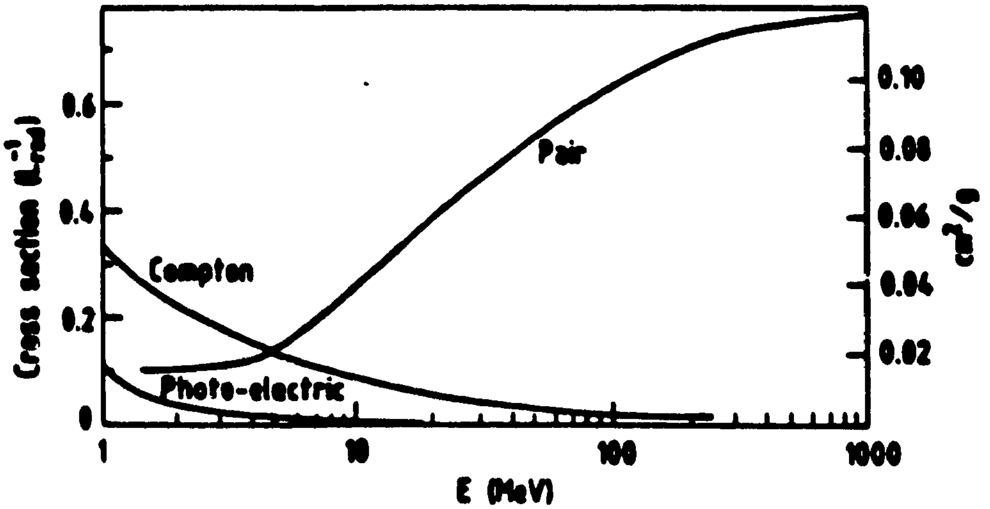

Figure 2.2: *Photon cross-section in lead as a function of photon energy. (from Rev. of Part. Prop. 1980 edition)*

energy ϵ_c can be parametrized by [10]

$$\epsilon_c \approx \frac{800}{Z+1.2} \; [MeV].$$

We describe the longitudinal and transverse development of a shower in terms of radiation length and of Molière radius. The radiation length, X_0, of a material is the distance a high energy electron must travel for its energy to drop to $1/e$ of its original energy purely due to bremsstrahlung. It can be approximated by [11]

$$X_0 \approx 180A/Z^2 \; [g/cm^2].$$

The average distance a very high energy photon travels before splitting into an e^+e^- pair is 9/7 X_0. The Molière radius, R_M, is a measure of the radial development of an EM shower. Most of the contribution to the radial spread comes from multiple scattering of the electrons. 95% of the total energy of a shower is contained in a cylinder of radius approximately 2 R_M. It is roughly given by

$$R_M \approx 7A/Z \; [g/cm^2].$$

For a DU-scintillator calorimeter, the Molière radius is about 2 cm.

The average amount of energy deposited at a given depth from the face of a calorimeter by EM showers can be parameterized according to [12]

$$\frac{dE}{dz} = E\frac{b^{a+1}}{\Gamma(a+1)}z^a e^{-bz}.$$

Here the constants a and b have a logarithmic dependence on energy :

$$a = a_0 + a_1 \ln E$$

$$b = b_0 + b_1 \ln E,$$

where for the ZEUS calorimeter the values are: $a_0 = 1.15$, $a_1 = 0.54$, $b_0 = 0.395/X_0$, $b_1 = 0.022/X_0$, E is in GeV and X_0 is in cm [13]. Longitudinal shower profiles are shown in Figure 2.3 for electrons of energy 1, 20 and 75 GeV.

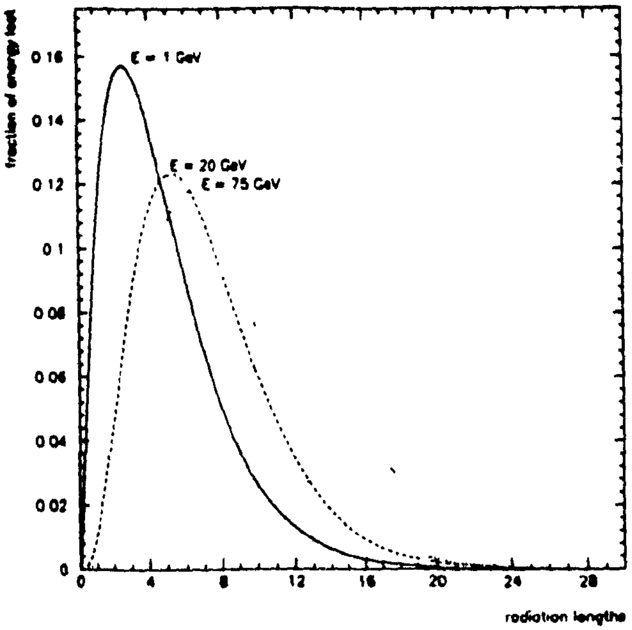

Figure 2.3: *Average deposited energy vs depth for electromagnetic showers of energies 1, 20 and 75 GeV*

2.1.3 Sampling fraction

The sampling fraction, defined as the fraction of a particle's energy deposited in the active layers, plays an important role in determining a calorimeter's resolution. This sampling fraction, R, of a particle is given by

$$R = \frac{E_{vis}}{E_{vis} + E_{invis}},$$

where E_{vis} is the energy deposited in the active layers; E_{invis} is the energy deposited in the passive layers. The different types of particles produced in a shower have different sampling fractions. For electrons and hadrons we denote the sampling fraction by e and h respectively. Sampling fractions are usually compared to those of minimum ionizing particles (mip). These ficticious particles have a sampling fraction given by

$$mip = \frac{\sum t_{act} dE_{act}/dx}{\sum t_i dE_i/dx},$$

where i runs over all the different media; t_i is the thickness of a layer of medium i; dE_i/dx is the minimum energy loss per unit length in medium i, and act is the active medium. Muons have a sampling fraction close to a mip and are often used as mips.

For an electron the e/mip ratio is less than one. The reason is due to the different Z dependence of the cross sections of the various interactions occurring in an electromagnetic shower. In the course of an electromagnetic shower many low energy gammas are produced. For these photons the photoelectric effect is the dominant interaction. Since the cross section of the photoelectric effect goes as Z^5, they are predominately absorbed in the high Z absorber region. The resulting low energy electrons have a very short range and most do not reach the scintillator. The e/mip ratio for a DU/scintillator calorimeter is about .62 and is only slightly dependent on energy.

2.1.4 Hadronic Showers

Hadronic showers are created through the inelastic scattering of the strongly interacting hadrons and their secondary particles by the nuclei of absorber material. A wide variety of different particles are produced, with differing energy loss mechanisms. A summary of the particles found in the cascade is provided below.

- Charged hadrons such as K's, π's, and p's which lose energy through ionization.
- π^0's and η's produced from the decay of hadronic resonances. They decay into two γ's and deposit their energy in the form of electromagnetic showers.
- High energy neutrons produced in the intranuclear cascade during spallation.
- Low energy neutrons released through evaporation of excited nuclei.
- Low energy gammas produced in fission processes and thermal neutron capture.
- Neutrinos from particle decay.

We can define a nuclear interaction length, λ in a similar manner to to the radiation length. λ is the average distance a hadron travels before colliding with a nucleus:

$$\lambda = \frac{A}{N_A \sigma_{abs}},$$

where N_A is Avogadro's number; A is the atomic weight of the nucleus, and σ_{abs}, the nuclear absorption cross section, is proportional to $A^{.711}$ [14].

Then the average longitudinal profile of the energy deposition in hadronic showers can be written as

$$\frac{dE}{dz} = E\left(\alpha\frac{b^{a+1}}{\Gamma(a+1)}z^a e^{-bz} + (1-\alpha)ge^{-gz}\right),$$

where a and b have the same values as in EM showers[15]. For a model of the ZEUS calorimeter $\alpha = 0.16$, $g = g_1 + g_2 \ln E$, $g_1 = 2.86/\lambda$ and $g_2 = -0.50/\lambda$ and $\lambda = 23.6$ cm.

The transverse dimension of a hadronic shower grows logarithmically with the energy of the shower. The width, W, needed to contain 99% of a shower in an iron-liquid argon calorimeter is [16]

$$W(E) = -17.3 + 14.3 \ln E \; [cm].$$

The particle diversity causes the resolution to be worse than pure electromagnetic showers. Each type of particle has its own sampling fraction. Neutrinos and some of the neutrons will totally escape the calorimeter without being detected. Also, the energy loss in breaking up the nuclei is not seen. Heavy charged particles will deposit energy through ionization similar to a mip. The π^0's and the η's have only a fraction of a mip's signal. The fluctuations of the proportions of particle types and the intrinsic fluctuations of hadronic showers are the main contributors to the energy resolution of hadronic calorimeters. The extra undetected energy losses cause e/h to be usually greater than 1.

A large source of fluctuations in a hadronic shower is the fraction f_{em} which is in the form of an electromagnetic shower. This fraction can vary widely from event to event with the production of high energy π^0's and η's early in the cascade. If the response from the electromagnetic and hadronic components of a shower are not the same, the resolution of the calorimeter to hadronic showers will be seriously degraded. Moreover, f_{em} is energy dependent and non-Gaussian.

2.1.5 Compensation

Due to the presence of the electromagnetically decaying π^0's and η's, hadronic showers have both an EM component and a nonelectromagnetic component. If the e/h ratio is not 1, the non-Gaussian fluctuations in f_{em} will cause σ_E/E to not improve as $1/\sqrt{E}$. At high energies the resolution will approach a nonzero constant term. In addition, the energy dependence of f_{em} causes e/h to be also energy dependent. This results in an alinearity in the calorimeter signal which could bias triggers based on energy because the detected energy of a single energetic particle would be different than that of a jet with the same total energy. Ignoring detector imperfections, the resolution of a hadronic calorimeter can generally be written as

$$\frac{\sigma}{E} = \frac{A\sqrt{t_{abs}}}{\sqrt{E}} + B(e/h - 1),$$

where t_{abs} is the absorber layer thickness, $A = ({\sigma^2}_{intr} + {\sigma^2}_{samp})^{\frac{1}{2}}$ is the contribution from intrinsic fluctuations, nuclear binding losses and sampling fluctuations and $B(0) = 0$.

In order to achieve $e/h = 1$ we have to compensate for undetected energy losses due primarily to the breaking up nuclei. We can either suppress the calorimeter's response to the electromagnetic component of the shower or increase the response to the hadronic component. Most of the compensation is usually attained through augmenting the hadronic response. For example the use of depleted uranium plates increases the hadronic response due to the extra energy released during fission processes. However, the most significant factor in increasing the hadronic response is the amount of energy neutrons transfer to a hydrogenous medium. It turns out that in the final stages of a shower's development most of the shower's energy is spent on nuclear processes. Low energy neutrons, protons and gammas are produced. Many more neutrons than protons are released, especially in large Z materials. These soft neutrons are eventually recaptured and lose their energy invisibly through elastic scattering. However, if the calorimeter contains hydrogen in the readout material, much of this lost energy will be recovered. The neutrons can transfer a large proportion of their kinetic energy to hydrogen, producing recoil protons. These low energy ($\sim$ 1 MeV) protons have a very short range and because they originate in the active material, they are not sampled. Instead, they will deposit all their energy in the active calorimeter layers. However, saturation of the medium can limit the extra light contribution from the ionizing protons. This is parametrized by Birks law,

$$\frac{dL}{dx} = A\frac{dE/dx}{1 + kBdE/dx}\ [cm^2/g].$$

where L is the light yield; A is the absolute scintillation efficiency; kB is a parameter relating the density of ionization centers to dE/dx. Nevertheless, the net result is a decrease in the e/h ratio. The amount of compensation can be chosen by varying the relative thicknesses of the active and passive layers of the calorimeter, or by adjusting the fraction of hydrogen atoms in the sampling medium. A final adjustment can be done by changing the signal integration time which determines what fraction of delayed gammas from neutron capture contribute to the signal. The e/h ratio can also be reduced by lowering e. This is done by inserting a low Z foil between the active and passive layers. This prevents photoelectrons produced at the boundary of the high Z material from reaching the active layers.

Compensation has been achieved for uranium/scintillator and lead/scintillator sampling calorimeters. In order to be compensating, a DU/scintillator calorimeter must have a scintillator/uranium volume ratio of about 0.82. The volume ratio is about 0.25 for a scintillator/lead calorimeter. This means that a compensating lead/scintillator calorimeter of the traditional layer type sampling variety would suffer from larger sampling errors than the DU/scintillator variety if normal scintillator thicknesses were used. Partial compensation has been achieved using liquid argon. In this case neutrons transfer their energy to argon in the same way they do with hydrogen, but with much less efficiency. At most only 10% of the neutron's energy is given to the recoil argon atom and this also occurs with a lower cross section[8]. It is also possible to improve the resolution of noncompensating calorimeters by estimating the fraction of energy deposited through π^0 decay and then applying weighting algorithms. This would require a fine longitudinal separation in the readout and was first attempted by the CDHS experiment[17].

The hadronic energy resolution of a compensating DU/scintillator calorimeter is the quadratic sum of its intrinsic and sampling resolution :

$$\frac{\sigma(E)}{E} = \frac{22\%}{\sqrt{E}} \oplus \frac{0.09\sqrt{\Delta E(1 + 1/N_{pe})}}{\sqrt{E}},$$

where E is in GeV, ΔE is the energy loss per layer in MeV and N_{pe} is the number of photo-electrons seen in the phototube. This yields an energy resolution for a typical calorimeter of $\sigma(E)/E = (33\% - 35\%)/\sqrt{E}$.

2.2 The ZEUS Calorimeter

Motivated by the need for a high resolution calorimeter to satisfy the physics requirements, the ZEUS collaboration began undertaking in 1985 design studies for a depleted uranium - scintillator calorimeter. Only after an extensive program with test calorimeters and Monte Carlo studies was the design finalized [18]. The sampling thickness in the EMC and HAC section was chosen to be 1 X_0 leading to a DU plate thickness of 3.3 mm.

The DU plates are fully encapsulated by a stainless steel foil of 0.2 mm thickness in the EMC and 0.4 mm in the HAC. The steel foil allowed safe handling of the DU plates during construction (the main concern was uranium dust), as well as a reduction of the signal contributed by the DU natural radioactivity. This radioactive signal (UNO) has to be low to minimize noise and radiation damage to the scintillators but large enough to be used for intertower calibration. The choice in DU plate thickness required a scintillator layer thickness of 2.6 mm to achieve $e/h = 1$.

The scintillator used is SCSN-38. It has a high light yield, low light attenuation and good stability against aging and radiation. The use of plastic scintillator with its fast decay time of the order of a few nanoseconds allows a very good timing resolution. This is important in reducing the background from cosmic ray and beam gas events. The fast response also alleviates pileup problems arising from the short interbunch crossing time. The composition and properties of the sampling layers are presented in Table 2.1.

The EMC section is made of 25 DU/scintillator layers. It is followed by the HAC1 section and ,in FCAL and BCAL only, the HAC2 section, each with up to 80 layers. Aside from the ^{60}Co sources, the calorimeter uses two other calibration systems. The UNO mentioned above allows the normalization of the signal from tower to tower without having to subject every tower to a test beam. Test results have shown that e/UNO (the ratio between an electron's signal at a given energy and the UNO signal) between different calorimeter towers is constant to within 1.1% in FCAL and 1.5% in RCAL[19]. The other calibration system uses pulsed laser light fed to the base of the light guide by optical fibres to monitor the linearity and long term stability of the photomultiplier tubes.

The calorimeter subcomponents are divided into modules. BCAL is made from 32 identical modules. FCAL and RCAL each contain 24 modules, two of which are half and positioned above and below the beam pipe. A summary of the dimensions of the modules in FCAL and RCAL is given in Tables 2.2 and 2.3.

Each FCAL/RCAL module is 20 cm wide and has a height varying from 2.2 to 4.6 m depending on its position to the beam. Thus the number of towers in a module ranges from 11 to 23. Figures 2.4 and 2.5 shows the positioning of the FCAL and RCAL modules.

2.3 FCAL/RCAL Modules

The modules for FCAL and RCAL were assembled by the Netherlands and Canada [19][20][21]. Each consists mainly of a stack of depleted uranium plates and scintillator tiles supported by a steel C-frame (see Figure 2.6). The C-frame has three parts, the end beam and the upper and lower C-arms. The end beam supports the stack of scintillator and DU plates during assembly and transport. Running along the end beam are two trays housing the optical fibre bundles for the laser system and the

material	thickness [mm]	thickness [X_0]	thickness [λ]
EMC			
steel	0.2	0.011	0.0012
DU	3.3	1.000	0.0305
steel	0.2	0.011	0.0012
paper	0.2		
scintillator	2.6	0.006	0.0033
paper	0.2		
contingency	0.9		
sum	7.6	1.028	0.0362
effective X_0		0.74 cm	
effective λ		21.0 cm	
effective R_M		2.02 cm	
effective ϵ_c		10.6 MeV	
effective ρ		8.7 g/cm^3	
HAC			
steel	0.4	0.023	0.0024
DU	3.3	1.000	0.0305
steel	0.4	0.023	0.0024
paper	0.2		
scintillator	2.6	0.006	0.0033
paper	0.2		
contingency	0.9		
sum	8.0	1.052	0.0386
effective X_0		0.76 cm	
effective λ		20.7 cm	
effective R_M		2.00 cm	
effective ϵ_c		12.3 MeV	
effective ρ		8.7 g/cm^3	

Table 2.1: *Composition of a Sampling Layer in EMC and HAC*

FCAL module type	F1T	F1B	F11	F12	F21	F22	F3	F4	F5	F6
no. of modules	1	1	2	8	2	2	2	2	2	2
active height (cm)	220	220	460	460	420	420	380	340	300	220
no. of 20x20 cm^2 towers	11	11	23	23	21	21	19	17	15	11
no. of 5x20 cm^2 EMC sections	36	36	76	68	52	44	36	12		
no. of 20x20 cm^2 HAC0 sections	2	2	4	6	8	10	10	14	15	11
no. of 20x20 cm^2 HAC1,2 sections	22	22	46	46	42	42	38	34	30	22
no. of EMC channels	72	72	152	136	104	88	72	24		
no. of HAC channels	48	48	100	104	100	104	96	96	90	66
maximum depth (λ)	7.1	7.1	7.1	7.1	7.1	7.1	6.4	6.4	5.6	5.6

Table 2.2: *Summary of the dimensions of FCAL modules*

RCAL module type	R1T	R1B	R11	R12	R21	R22	R23	R3	R4	R5	R6
no. of modules	1	1	2	6	2	2	2	2	2	2	2
active height (cm)	220	220	460	460	420	420	420	380	340	260	220
no. of 20x20 cm^2 towers	11	11	23	23	21	21	21	19	17	13	11
no. of 10x20 cm^2 EMC sections	9	18	38	34	30	26	22	18	6		
no. of 20x20 cm^2 HAC0 sections		2	4	6	6	8	10	10	14	13	11
no. of 20x20 cm^2 HAC1,2 sections	11	11	23	23	21	21	21	19	17	13	11
no. of EMC channels	18	36	76	68	60	52	44	36	12		
no. of HAC channels	22	22	54	58	54	58	62	62	62	26	22
maximum depth (λ)	4.0	4.0	4.0	4.0	4.0	4.0	4.0	4.0	4.0	3.3	3.3

Table 2.3: *Summary of the dimensions of RCAL modules*

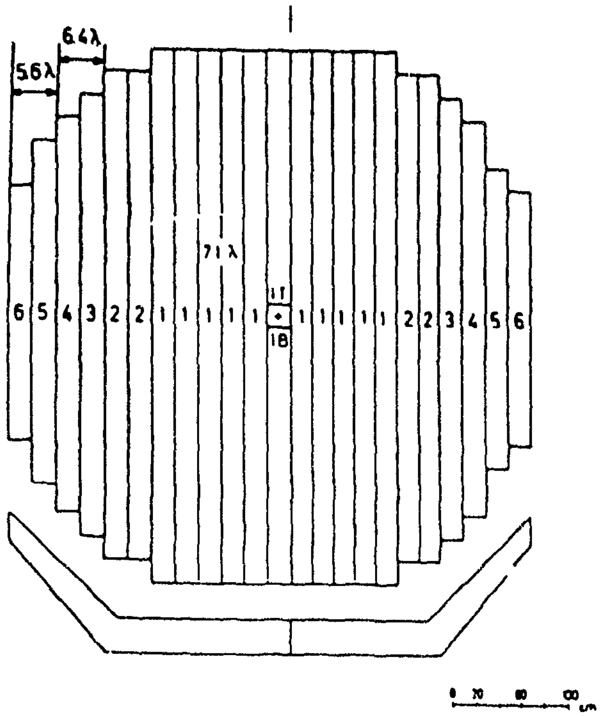

Figure 2.4: *Positioning of FCAL modules*

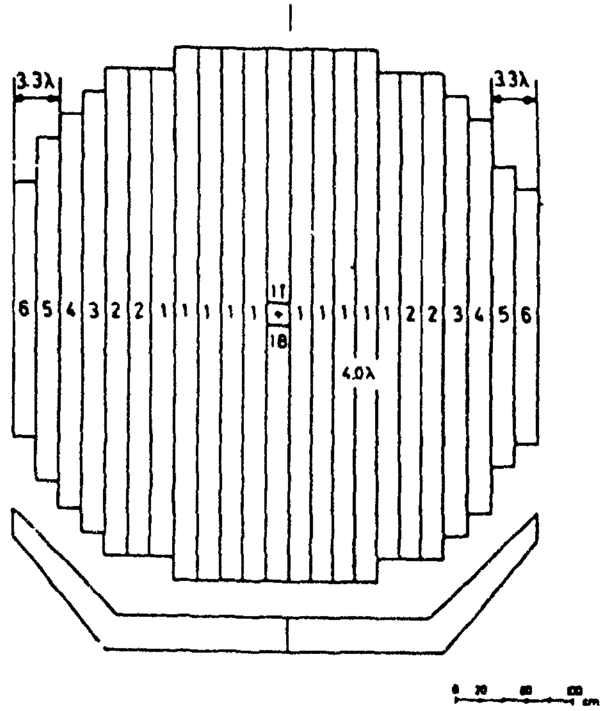

Figure 2.5: *Positioning of RCAL modules*

brass pipes for ^{60}Co calibration. Access to the fibre bundle and source pipes is via the upper C-arm. When the module is finally installed it rests completely on the lower C-arm.

2.3.1 DU/scintillator stack

Depleted uranium is an alloy consisting of 98.4% ^{238}U, $\leq 0.2\%$ ^{235}U and $1.4\% Nb$. It has a density of about 18.9 g/cm^3 with a radiation length of 3.2 mm and a nuclear absorption length of 10.5 cm. The DU plates are 3.3 ± 0.2 mm thick, and 188.8 mm wide in the EMC section, 183.8 mm in the HAC1 section and 178.8 mm in the HAC2 section. The plates were limited by production methods to only ~ 3 m long so it was necessary to weld two together for the larger modules. They are surrounded by a layer of .2 mm thick steel foil. Those in the HAC sections have a second layer to further reduce the DU noise.

At the front of the DU/scintillator stack is a 15 mm thick aluminum front plate with the edges smoothed to allow the steel straps compressing the stack to slide. Immediately behind the plate lies first a scintillator layer and then 25 layers of DU/scintillator of the EMC section. After the fourth scintillator layer (and also after the 7th in FCAL) is a 15 mm gap for the silicon HES detectors. A thin steel sheet keeps the scintillator tiles from falling into the gap. The first scintillator tile has no DU plate before it because the dead material in front of calorimeter (from the solenoid, tracking detectors, and front plate) already contributes about a radiation length of absorber.

The scintillator material, SCSN-38, is an aromatic plastic with a cross linked polystyrene base doped with two wavelength shifting dyes, butyl-PBD (1%) and BDB (0.02%). The scintillators tiles were saw cut and machine polished on all four edges. They have a thickness of 2.6 mm ± .2 mm. This thickness distribution is shown in Figure 2.7. The tiles were selected such that the those closest to 2.6 mm thick were used in the EMC sections. This was to help give the EMC sections, which had only 26 scintillator layers, the best uniformity. The 4 EMC tiles in a layer of a FCAL

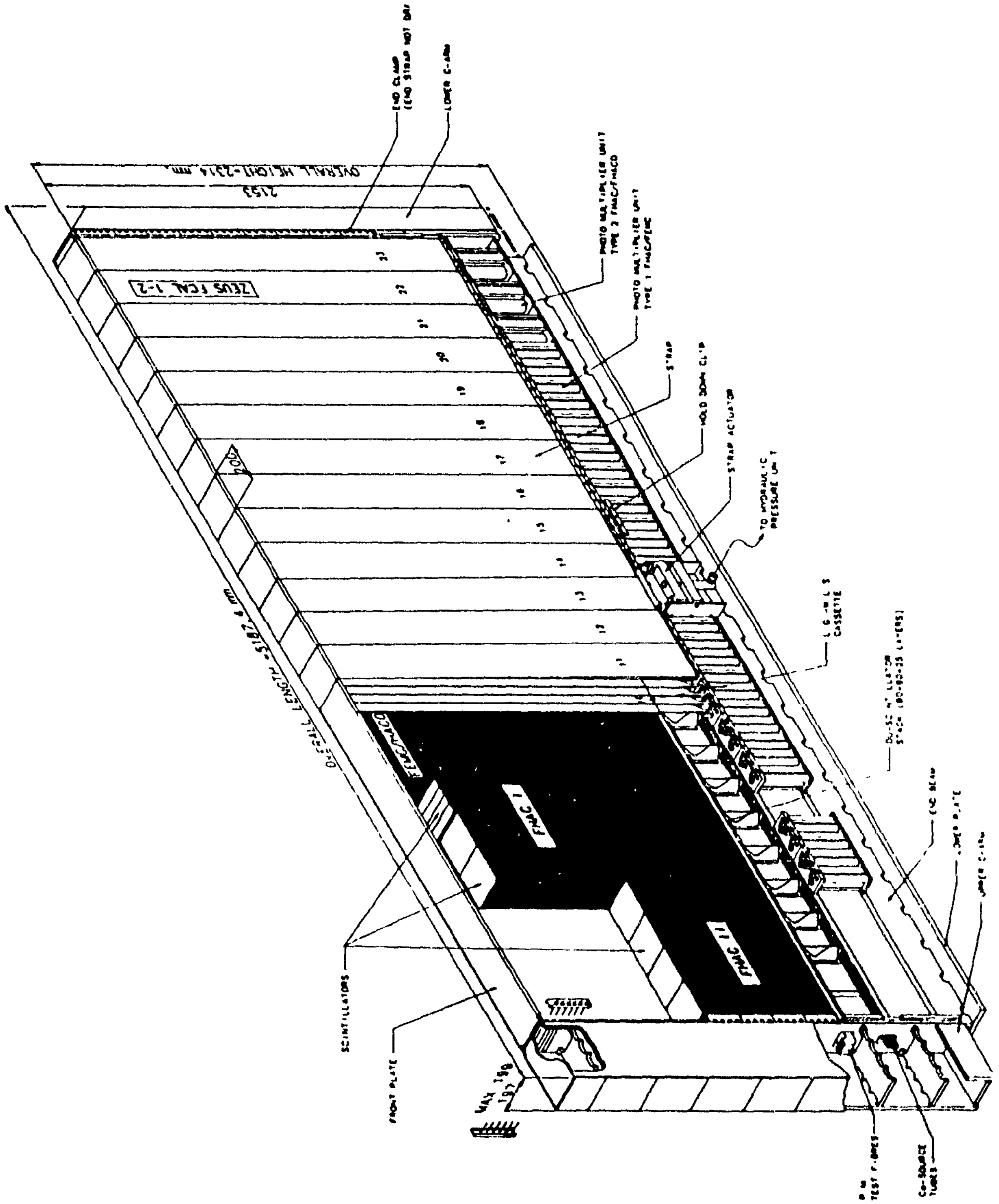

Figure 2.6: *View of a Large FCAL Module*

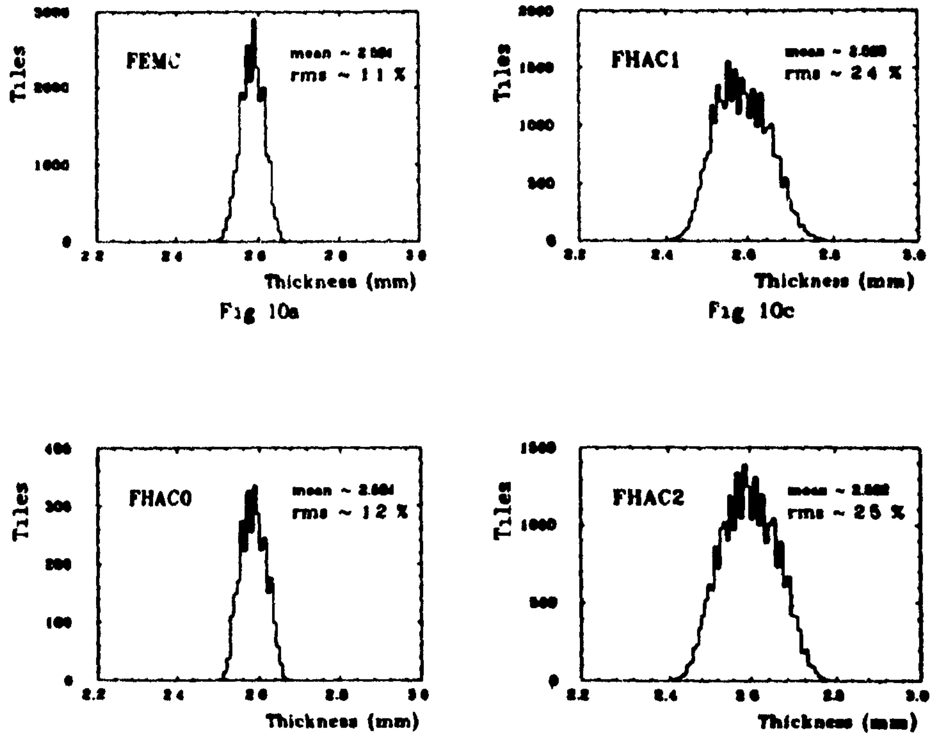

Fig 10a Fig 10c

Fig 10b Fig 10d

Figure 2.7: *Thickness Distribution of FCAL scintillators*

tower are labelled EMC1, EMC2, EMC3, and EMC4 with EMC1 being closest to the bottom C-arm. In RCAL the EMC tiles are similarly labelled EMC1 and EMC2.

The DU plates are kept separated by tungsten carbide spacers positioned every 20 cm along the edge of the plates. Because there is less weight to support in the EMC sections, it was possible to use there titanium carbide spacers whose lower Z reduces their effect on shower development. To accommodate the spacers all the scintillator tiles except the EMC2 and EMC3 tiles in FCAL have cutouts at the corners.

To improve the uniformity of response from the scintillator tiles, they were wrapped with white and black patterned Tyvek paper 0.18 mm thick. The Tyvek paper is kept in place by two black Tedlar sleeves at the readout edges. This keeps the uniformity of response to within ± 2% in the EMC and ± 4% in the HAC over 95 % of the scintillator area. Figure 2.8 shows the pattern used for the FCAL EMC scintillator tiles. The patterns were coarse enough such that only one type was needed for each type of scintillator.

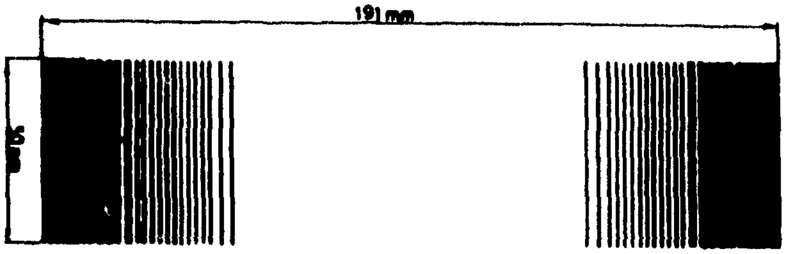

Figure 2.8: *Tyvek Paper Pattern used for FCAL EMC Scintillators*

2.3.2 Optical Readout

The optical readout consists of WLS plates and light guides transporting the scintillator light to the PM tubes where it is converted to an electrical signal (see Figure 2.9). The WLS is a 2.0 mm ± 0.2 mm thick plate made from polymethyl methacrylate (PMMA) doped with the fluorescent dye Y-7 and an ultraviolet absorbant. The UV absorbant cuts off wavelengths below 360 nm. This was intended to reduce the contribution to the signal from Cerenkov light produced by showers occurring in the cracks between modules. In the EMC and HAC0 sections the Y-7 concentration is 45 ppm. All other sections use a concentration of 30 ppm. The higher concentration of Y-7 in the EMC WLS increases the light yield by absorbing more of the scintillator light before it passes out of the WLS and scatters off the back reflector (see below) The Y-7 dye allows the WLS to bring some of the scintillator light through the ninety degree turn to the PM by absorbing the blue scintillator light and re-emitting it isotropically[22]. The light guide at the end of the WLS is made of bent strips joining the rectangular end of the WLS to the circular surface of the PM photocathode. The light guide transports the light from the WLS to the PM adiabatically by transforming the cross sectional surface of the WLS from a long thin rectangle to a

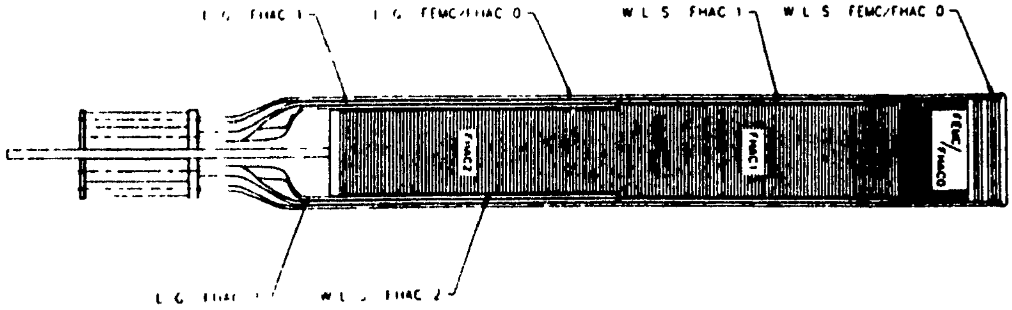

Figure 2.9: *View of WLS reading out scintillator*

square matching better the photocathode surface, while maintaining the same cross sectional area. The light guide and WLS plate are made as one piece in order to avoid light losses from glue joints.

To help optimize the uniformity of response 'end reflectors' and 'back reflectors' made from aluminized foil were added. The end reflector positioned at the end opposite the light guides reduces the attenuation and significantly increases the total light yield. The response of each wavelength shifter was measured and an individualized pattern of either black dots or black lines was applied to the back reflector to reduce the position dependence. The final uniformity of the WLS was within ±3%. The WLS plates reading out all the sections for one side of a tower are mounted in a cassette made from 0.2 mm thick stainless steel. Between the EMC plates lie the brass tubes used in the cobalt scanning, 2 per cassette in FCAL and only 1 per cassette of RCAL. Foam rubber between the cassette and WLS pushes the WLS against the scintillator tiles. However, direct contact between WLS and scintillator which could cause partial optical contact is prevented by 0.4 mm thick nylon fishing lines.

In the final stage of the optical readout system the WLS light is collected by the photomultiplier tube. A PM consists of a photo-cathode which emits electrons when struck by photons. These 'photoelectrons' are accelerated by an electric field through a series of dynodes set at increasing voltage. Upon striking a dynode an electron will release many more electrons which are all accelerated to the next dynode. This multiplicative effect amplifies the signal such that only a few photons are needed to strike the photocathode to produce a measurable signal. The PM tubes are required to have good gain stability, good linearity over the entire dynamical range and small dark current. The XP1911 tube from Philips was chosen for the EMC sections of FCAL and the R580 tubes from Hamamatsu Photonics for the rest. Both types are 10 stage head-on tubes with diameters of 19 and 38 mm respectively. They have bi-alkaline photocathodes with a spectral response matching well the spectrum of Y-7 dye in the WLS. The tubes are equipped with Cockcroft-Walton bases to supply the high voltage. These bases step up the voltage internally, dissipating less heat than resistive bases and requiring a maximum external voltage of only 24 V.

2.3.3 Straps

The DU/scintillator stack and WLS cassettes are kept together by .25 mm thick steel straps each 196 mm wide, one for each tower. The straps are tensioned to a force of 15-20 kN per tower. The straps press onto the aluminum front plate and are fixed below the frontplate of the endbeam via bulkheads to the photomultiplier housing assembly. The gaps between the straps as well as cracks leading to the optical readout system were covered with metal tape and black tape to prevent outside light from leaking in.

Chapter 3

^{60}Co Source Scanning

The short term goal of the ^{60}Co scans was to discover construction imperfections which would affect the response uniformity of the calorimeter. This was possible by taking advantage of the relatively limited range of the emitted gammas which illuminated only a few layers at a time. Local information about the structure of the calorimeter stack and the response of the WLS could be obtained. The scans were done before installing the modules into the ZEUS detector in order to have time to repair them, if possible. It will also be used as a long term monitor of the characteristics of the optical components such as the WLS uniformity and scintillator attenuation length. Plastics, used as the base material for scintillator and WLS, are vulnerable to damage from aging and radiation, causing them to turn yellow and producing minute surface cracks (crazing) which degrades their optical qualities. This decreases their attenuation length and reduces their light yield. Because the scintillator layers closest to the interaction region receive more radiation, a variation in the light output efficiency from one layer to the next can occur. Such a nonuniformity in the optical readout, whether from radiation damage or intrinsic to the construction, would increase the sampling fluctuations and worsen the energy resolution. More importantly, since the longitudinal shower profiles are energy dependent, the nonuniformities could cause the absolute energy calibration of the calorimeter to be nonlinear. For example, it has been estimated that to keep the barrel calorimeter response variation under 1%

for electrons in a range of energies 1-100 GeV in the EMC section, the nonuniformity in the WLS must be less than 7.2%.[23]

In order to conduct scans with radioactive sources, the source must somehow be brought into close proximity with the scintillators. Since the modules, once installed, are packed as closely as possible side by side to minimize dead space, the delivery system has to be interior to the modules if any scans are to made after the ZEUS experiment begins. Because there is no space available within the DU/scintillator stack (drilling holes in the plates and tiles would have had serious side effects), the source has to travel either in or beside the WLS cassettes. Tubes are an obvious choice to use to guide the source. If we want to scan each EMC section in the same way, a minimum of two tubes (each between a pair of EMC WLS) are required per FCAL cassette and only one per RCAL cassette. The tubes which run down the WLS must somehow be accessible from the outside. This is only possible through the upper C-arm. Therefore the tubes are forced to undergo a ninety degree turn in order to reach the C-arm. Using the C-arm does however offer the advantage that all tubes can be accessed from one location in the module. The source itself should be small to provide fine detail on the layer structure. To bring it in and out of the tubes, it has to be attached to a wire or rope of some sort. The 90° bend in the tubes requires a wire flexible enough to bend without kinking, but stiff enough to pushed through a vertical bend. These were the design considerations.

In the end two different procedures were used in conducting source scans, one with the source inside the module (inside scanning), the other with the source outside (outside scanning). At first, inside scanning was performed at CERN and at DESY on a few large FCAL modules, where a radioactive ^{60}Co source at the end of a piano wire was inserted into tubes running along the WLS inside the module. The signals from the PMs were read out as the source wire was slowly pulled out by a computer controlled driver. After an accident with the inside scanning, adjustments were made so that all modules were scanned on a preparation stand by a source wire inserted into tubes mounted on a movable platform outside the module.

^{60}Co was chosen as the radioactive source to scan the modules because of its energetic gammas, long lifetime and ease of handling. It emits gamma rays at two energies, 1.173 and 1.332 MeV, in equal proportions. Gamma sources are superior to electron sources because low energy electrons have a very short range and would stop in the WLS before reaching the scintillator. A lower energy gamma source would have the advantage of illuminating fewer layers at at time, but the reduced penetration depth could also increase the scan's sensitivity to effects arising from scintillation light being produced very close to the scintillator edge. ^{60}Co's long lifetime of 5.271 years relieves the necessity of frequently making new sources. Only one source was needed to scan all the modules over a period of six months.

3.1 Physics of Light Production

In the energy region around 1 MeV, the dominant interaction of photons is Compton scattering (c.f. Figure 2.2). The energy transferred, E_k, to the electron in Compton scattering can be expressed as a function of the scattering angle, θ, by

$$E_k = \frac{E_\gamma^2}{m_e c^2} \frac{1 - \cos\theta}{1 + \frac{E_\gamma}{m_e c^2}(1 - \cos\theta)}.$$

For a γ with an energy of 1.332 MeV, the maximum energy transferred is 1.038 MeV (for $\theta = 180°$).

Some of the energy deposited in the WLS by the fast electrons produced from Compton scattering is re-emitted by the excited atoms in the form of Cerenkov light. Electrons travelling in a dielectric material with an index of refraction n will produce Cerenkov light if their velocity is greater than c/n, the speed of light in the medium. The amount of energy emitted as Cerenkov light with a wavelength, λ, is given by

$$\frac{d^2E}{dx d\lambda} = 4\pi^2 r_e mc^2 \frac{1}{\lambda^3}\left(1 - \frac{1}{\beta^2 n^2}\right),$$

where r_e is the classical radius of the electron. Most of this light is absorbed by the ultraviolet absorber in the WLS, but some of the longer wavelength components may eventually travel down the WLS and contribute to the signal in addition to that from the scintillator light.

All organic scintillators contain a benzene ring in their structure. The ionizing energy from a passing high energy particle excites free valence electrons. They then lose vibrational energy and the molecule ends up in a vibrational level of the first excited state without the emission of light. After a short period of time the molecule emits a photon, decaying to a vibrational level of the ground state before falling to the ground state. The net result is that scintillator is transparent to its own radiation. The two dyes used in SCSN-38 increase the attenuation length as well as shift the ultraviolet light from the base to a wavelength matching the absorption spectrum of the Y-7 in the WLS. Figure 3.1 shows the absorption and emission spectra of the dyes involved.

The light then travels via total internal reflection to one of two ends where it enters the wavelength shifter. Only light impacting the boundary between air and scintillator at an angle greater than $\theta = \arcsin(n_1/n_2)$, where n_1 and n_2 are the indices of refraction of air and scintillator respectively, will be reflected. For SCSN, $n = 1.48$ and $\theta = 42$ degrees. Of the light that is not reflected and passes out of the scintillator, most will be partially scattered by the Tyvek wrapping. Some of it which reenters the scintillator may be absorbed by the dyes and re-emitted in a direction such that it eventually reaches the WLS. The patterned back reflector of the WLS works in a similar way as the Tyvek paper. Some of the blue light from the scintillator passes through the WLS without being absorbed and re-emitted isotropically as green. The pattern on the back reflector controls how much of this light is reflected back into the WLS to have a second chance to be absorbed and re-emitted.

3.2 Inside Scanning

In FCAL the EMC towers have 2 brass guide tubes per side, one running between the EMC1 and EMC2 WLS, the other between the EMC3 and EMC4 WLS. For the HAC0 towers the tubes run along the spacer column, and for REMC they run between the EMC WLS strips. The tubes have an outer diameter of 2.5 mm and an inner of 2.0 mm. The tubes run straight to near the end of the light guide where they are each glued to an elbow. Figure 3.2 shows the region around the light guides where the elbow is located. The elbows join to long brass tubes lying on a tray along the web plate of the end beam. These tubes run towards the upper C-arm where they grouped together in an interface. A fanout lies in the top C-arm connecting the interface via brass tubes to holes arranged in a circle of a cover plate to which the driver is mounted. The driver is first attached to an extender which allows the driver to be located on the RCAL modules which are most restricted in space. The extender is an aluminum plate with a circle of short brass tubes projecting out. These tubes link with holes in the base plate of the driver. The extender is mounted to the fanout by four brass pegs and two long screws. The driver pushes the wire to the end of a selected brass tube. It then draws the wire out while data from the PMs is recorded onto disk.

The driver had difficulty inserting the wire to the end of the brass tubes due to the buildup of frictional forces. Often the wire had to be manually inserted past the elbow to the end of the brass tubes from where the run would be started. Some of the elbow joints were not properly glued and the source wire would pop them open. The wire would then exit the elbow and be pushed underneath the straps. This caused kinking in the wire. The damage to the source wire eventually prompted the development of an alternate interim scanning method (see below).

3.3 Outside Scanning

An accident occurred while scanning module NL4 with a repaired source using the inside tubes. The source wire broke off at the repaired joint and was left behind in the module when the wire was removed. The source was recovered, but had this happened after the module had been installed in the ZEUS detector, its recovery would have required the removal of the module. Further inside scanning was suspended until some method to assure that such accidents would not be repeated was found.

A new method with using a driver and straight guide tubes mounted on a movable platform outside the module was implemented in order to continue the source scans. A modified source driver was attached to a movable platform on rollers. The driver was positioned on top (over the aluminum front plate) of a tower. Two aluminum wings containing brass guide tubes hung from the platform, one on each side, down the length of a tower. Two different pairs of wings were made, one for FCAL and one for RCAL. The wings were 20 cm wide and 12 mm thick. The FCAL wings have 4 brass tubes per side spaced 5 cm apart. The RCAL wings have only 2 tubes per wing spaced 14 cm apart. In addition, one wing from each pair has an additional tube used for loading and unloading the source wire. These tubes had only a very slight bend in going from the driver to the wings and no joints.

For the FCAL modules the platform was positioned such that the outer brass tubes were positioned over the inner ones. In an attempt to position the wings accurately, they were fixed in place by aluminum profiles screwed to holes in the PM mounting.

The RCAL wings were positioned by eye using the gaps between the straps as a guide directly over EMC towers or straddling two HAC0 towers. They were fixed in place by a wedge between the wing and the crossbars used to support the module during transportation. Since the source tubes were 3 cm from the nearest end of the scintillator, a very precise positioning was not necessary.

3.4 The Source Wire

A number of different source designs were tested in the prototype calorimeter. Two source wires of the same design were used in the inside measurements. After being damaged one was later modified and used as the source wire for the outside scanning. The original source wires (Figure 3.4) used in the inside measurements were manufactured by DuPont, and consisted of a nickel plated ^{60}Co source $\sim$1.0 mm long, with a diameter of 0.7 mm at the end of 0.76 diameter 8 m long piano wire. The source was dropped into a 2.13 m stainless steel tube of 1.1 mm outer diameter and 0.8 inner diameter which had had its end welded closed. The wire was inserted and pushed the source to the closed end. The other end was hard soldered to the piano wire. The length of the tube meant that the joint did not have to enter the elbow region of the brass tubes. Both wires were kinked in the course of scanning. An attempt to repair one was made by cutting off the wire 60 cm from the tip and joining it to another wire with a short soldered sleeve. This was not successful as the repaired wire eventually broke just above the sleeve while in a guide tube. The source wire used for outside scanning was made from the second damaged wire. The tip of the old wire was cut off, with the cut end soldered flat, and dropped down a 1.5 mm outer diameter stainless steel tube approximately 3 m long. The end of the tube had previously been closed by soldering to it a plug of hardened carbon steel. A 1.2 mm diameter piano wire 5 m long was inserted into the other end and pushed as far as possible to bring the source close to the closed tip of the tube. The piano wire was then soldered to the end of the tube. Because the source was disjoint from the piano wire, a weak point in the steel tube was created where the source and piano wire met. This was done deliberately because it ensures that if the tube were to break, it would break away from the tip and not damage the source.

The problem with this design stemmed from the nonuniformity of the source wire due to the soldered joint connecting the steel tube to the piano wire. It was often difficult pushing the wire into the tubes past the elbow. The reason for this is that because the piano wire is more flexible than the steel tube, it bunches up, increasing the friction with the brass tube. This could be solved by using a longer length steel tube covering the entire piano wire.

The source's activity of 2 mCi was chosen so that the signal from the ^{60}Co source would be roughly the same as that from the uranium noise.

Distance from source [cm]	Calculated Dose for a 2 mCi activity ^{60}Co source
7	5510 $\mu Sv/h$
15	1200 $\mu Sv/h$
60	75 $\mu Sv/h$
80	42 $\mu Sv/h$
100	27 $\mu Sv/h$
120	16 $\mu Sv/h$

Table 3.1: *Radiation Dose from a 2 mCi ^{60}Co source vs distance*

3.5 Safety

Of a rather major concern are the safety aspects of using a strong radioactive source. The tip of the source wire was kept in a lead 'pig' and the wire was fixed with a clamp when not in use. Even then the radiation dose at the surface of the pig was 100 μSv/hr requiring the pig to be stored in a large cabinet and surrounded by lead bricks. Table 3.1 shows the calculated radiation dose for a 2 mCi source at various distances. As a comparison, the radiation dose from the uranium of a module is 42 μSv/hr at the surface. The average dose from natural background radiation is about 2 mSv per year. We see that at a distance of slightly less than a metre, the radiation from the source is approximately the same as that from the surface of a module. The outside scanning procedure was rather safe. The control hut, from where the run control was operated, was several metres from the module stand. Close exposure to the source could only occur if one was not careful during the loading and unloading of the source, or if for some reason the source was unable to enter the tubes and had to be manually aided.

3.6 Preparation

The scanned modules were set up in a preparation stand with the faces of the towers facing upwards where they were first checked for light tightness and defective PM tubes. The high voltage to the Cockcroft-Walton bases of the PM tubes was provided by 16 channel CAMAC controllers which also read the monitoring voltage. Each controller included a 12 bit DAC to supply the voltage and a 12 bit ADC to read the monitoring voltage. These photomultiplier high voltages were set such that signal from the uranium noise would be the same for similar sections of every tower. This was done through autotrimming. By knowing certain parameters of the PM's base it is possible to iteratively reach a desired gain. The correct high voltage for a requested integrator value from UNO can be found after only a few iterations. The typical HV on a PM was about 1100 V. The UNO values for the FCAL EMC PMs were set at one fifth of the HAC PMs. The HAC0 towers, with four times the surface area of the EMC towers had their UNO values set at four times the EMC values. The PMs were left alone for a few hours to stabilize their signals. After every few towers had been scanned a new UNO run was taken. The UNO values recorded were actually the average over 500 measurements. There was effectively no difference between inside scanning and outside scanning as far as the driver and data acquisition systems were concerned. Once the driver was in place the procedure of pushing in and pulling out the source wires was common to both methods.

3.7 Scan sequence

Once the driver was in place and the source wire loaded, scanning could start. The operator entered the tower(s) and tube type(s) to be scanned to run control program. The program then looked up in a database the correct tube number and tube length. This would be relayed to a microprocessor which would handle from then on the actual movements of the source. The driver would then position the source over the entrance to the correct tube. The source wire was pushed into the tube in 5 stages[26]:

stage 1: The source is pushed down 60 mm at its slowest speed of 4.4 mm/s. This ensures that the source moved safely through the connections into the fanout.

stage 2: The source travels at 60 mm/s until it reaches a distance tube length - 2000 mm (before the elbow in FCAL).

stage 3: The source moves a distance of 400 mm around the bend at 20 mm/s.

stage 4: The source continues on at 40 mm/s until it reaches about 50 mm from the end.

stage 5: The source goes at 4.4 mm/s until it reaches the tube end. At this point the run starts.

The microprocessor then informs a MVME-135 computer using the OS-9 operating system (this computer will subsequently be referred simply as the OS-9) that the run can start and proceeds to draw the wire out at its slowest speed. Meanwhile the OS-9 occupies itself with taking data. It receives only status information and position updates from the microprocessor. Once a run is over and the source wire is back in a standard 'home position', the microprocessor waits for further instructions from the OS-9.

3.8 The Driver

The source driver is driven by a stepping motor from the firm SIGMA and controlled by a Motorola microprocessor 68HC11 with a 6800/6801 cpu. The microprocessor runs a program written in FORTH downloaded from an OS-9 MVME-135 computer. They communicate via a RS-232 serial line. The microprocessor communicates with the stepping motor through a Superior Electric 430-PT motor translator which in turn generated the correct drive signals to operate the stepping motor. The motor translator requires four TTL levels from the microprocessor, controlling step mode (half/full), winding direction (clockwise/counterclockwise), motor power (on/off), and providing pulses signalling a step. The control layout is shown in Figure 3.6 The stepping motor can be set at either full step or half step mode, offering a choice of either 200 full or 400 half steps per revolution of the motor shaft. Movement of the driver is controlled by a variable speed interrupt generated square wave from the microprocessor. Two counters are set in the microprocessor with the second having a value WIDTH greater than the first, where WIDTH is the width of the desired pulse in clock cycles. When the microprocessor clock equals the value of the first counter, an interrupt occurs, setting an output port to the motor translator high. The counter is then advanced by a value PERIOD where PERIOD clock cycles is the desired period of the square wave. WIDTH cycles later a second interrupt occurs, toggling the output port low and the second counter is also advanced by PERIOD. The motor driver shaft turns one of a pair of rubber rollers pushing or pulling the source wire. With a rubber roller diameter of 2 cm, each half step moves the source wire 0.16 mm. The slowest velocity was obtained in half step mode, providing about 4.4 ±3% mm/s. The fastest velocity was obtained in full step mode, about 80 mm/s. The source driver could push the wire with a force of about 10 N. At lower velocities the motor provided more torque.

The layout of the driver is shown in Figures 3.7 and 3.8 The position of the source wire is followed by a REX-32 shaft encoder rotating with a second pair of rollers turned by the moving source wire. The encoder gives 400 pulses per revolution. They are sent to a 12-bit HCTL-2000 decoder chip on the microprocessor board. The decoder multiplies the number of pulses from the encoder by four, giving 1600 counts per revolution and writes it into memory for quick readout by the microprocessor. The microprocessor reads this value every 300 ms, checking if an overflow had occurred or if the source wire has stopped moving. The jitter of the decoder is less than 20 counts. Using 1 cm radius rollers, the count to distance conversion factor is 255.6 counts per cm. If the distance travelled since the last readout is not enough (about 1 mm at slow speed) the driver will continue trying for a few more readings before stopping, believing that either an obstacle or the end of the tube had been reached. The run could only start if the the source stopped no more than a few centimeters short from the requested distance to travel down the tube. The decoder was calibrated for 1 cm radius rollers moving the 1.1 mm wire used for the inside scanning. The source wire for the outside scanning had instead a thickness of 1.5 mm. Due to the extra compression the rollers used for outside scanning had an effective radius of only 9.8 mm. This introduced a scale error of about 2% in the distances recorded during outside scanning.

After scanning a tube the source wire was pulled out to 'home position' with the tip positioned a little before the rollers. A slotted optical switch located beneath the rollers would fire if it could not detect the presence of the source wire, stopping the motor. Without this optical switch the source could be pulled out, so it was important that the threshold of the switch be properly adjusted. The TTL signal from the switch could be monitored externally by a voltmeter.

Once in the home position, the driver would change to the next tube. The driver assembly moving the source wire was mounted on a dial which was the largest of three intermeshing gear wheels. Another stepping motor, identical to the first, and controlled in the same manner by the microprocessor, turned the smallest gear wheel. The gear ratios were 154:36:36. The dial lies just above the base plate of the driver assembly. The base plate has a ring of 100 holes equally spaced. The holes are labeled from -50 to 50 with 0 being home position for the dial and -50 and 50 representing the same hole. These holes lead to the short tubes of the extender. Not all holes corresponded to a brass tube in the module, but a map of the hole assignments was kept on the OS-9. The dial driver positioned the source driver over the appropriate tube. 16 half steps separated neighbouring tubes. Before changing to the tube for the next run the dial would first turn to its home position. Attached to the source driver's assembly was a metal finger which would trigger a second optical switch on the base plate when the dial was at the dial's home position. Then the dial would rotate to the next hole.

3.9 The outside driver

The driver used in the outside scanning was modified from the original driver used for inside scanning. The entire driver assembly was mounted about 40 cm above a platform equipped with two rollers with wheels on the end. The wheels rolled along the side of the module as the driver was moved from tower to tower. This gave the platform extra stability against tipping. Sitting on the platform underneath the dial's home position was a lead pig used for storing the source while the platform was moved to a new tower. Access to the pig was provided by a brass tube connecting to tube 0. Only nine other tube holes in the bottom plate of the driver assembly were used, four per side for scanning and one extra for loading the source wire. These holes lead to the brass tubes projecting from the aluminum wings. The tube database on the OS-9 was modified before every tower so that the run control program would use only these tubes to scan every tower. The free end of the source wire was guided through a 30 cm vertical brass tube immediately above the rollers and threaded through a high aluminum profile above the driver to help prevent sharp bends occurring in the wire near the source driver. A camera, mounted on this profile, was connected to a TV screen in the control hut to allow the operator to remotely monitor the operation of the source driver.

3.10 Data Acquisition

The readout electronics used in the ^{60}Co scans were based on those that will be used for the slow control during the ZEUS experiment. The signals from the PMs were collected by special integrators designed specifically for the ^{60}Co scans with an integration time of about 24 ms. During this time they would each receive $4 - 5 \cdot 10^5$ pulses. The integrators were read by 12-bit multiplexer analog to digital convertors (MUX-ADC) in a VME crate. Each MUX-ADC card has an ADC which read out 96 independent channels with a total readout time of at least 50 ms. In practice the time delay between consecutive readouts was 60 to 90 ms, due to the time needed to transfer the data to the OS-9. The range of the MUX-ADC was ± 5 V. Thus one ADC channel was about 2.5 mV. The UNO values were set at 500 mV for the FCAL EMC, 1000 mV for the RCAL EMC, 2000 mV for the HAC0, and 2500 mV for the HAC sections. The 90 ms readout rate meant that measurements were taken at 11 points per second. This corresponded to 2-3 measurement points per millimetre. The source position was updated in the data after every 10 measurements. The off line analysis programs interpolate between the recorded positions to obtain the true position of every data measurement. The raw data could be plotted on a terminal during the run. For data taken from inside scanning, distance was measured from the end of the tube by the front plate. For data taken during outside scanning, distance was measured from the end of the tube just past the last HAC section.

For every run up to 12 PMs were read out, 6 on each side of the module. The raw data were recorded in ZEBRA EXCHANGE format[27]. ZEBRA is a data management system supported by CERN. One run in FCAL took about 1.3 Mbytes of space. This data was later concentrated so that only the average per mm was kept [25][26]. In this way a run required only 180 kbytes of storage. A large FCAL module required about a hundred runs. The OS-9 had only about 80 Mbytes of disk space so the raw data was transferred over ethernet to the central DESY VAX where it was later concentrated and put onto magnetic tape for permanent storage.

The scanning time was about 40-50 minutes per tower, doing 2 tubes on each side. The data taking itself required only 6 minutes to scan the 1600 mm of a FCAL tower. The rest of time was needed for the source to reach the end of the tube, to change tubes and, in the case of outside scanning, to move the scanning apparatus to a new tower. The large FCAL modules took about 20 hrs each to scan, not including the preparation time for cabling, fixing light leaks, etc.

In scanning all of the FCAL and RCAL modules, some 5000 runs were taken, including repeated runs and special measurements. The raw data filled 40 magnetic tapes (6250 bpi), the concentrated data another five. The entire outside scanning operation occurred between October 1990 and April 1991 at DESY.

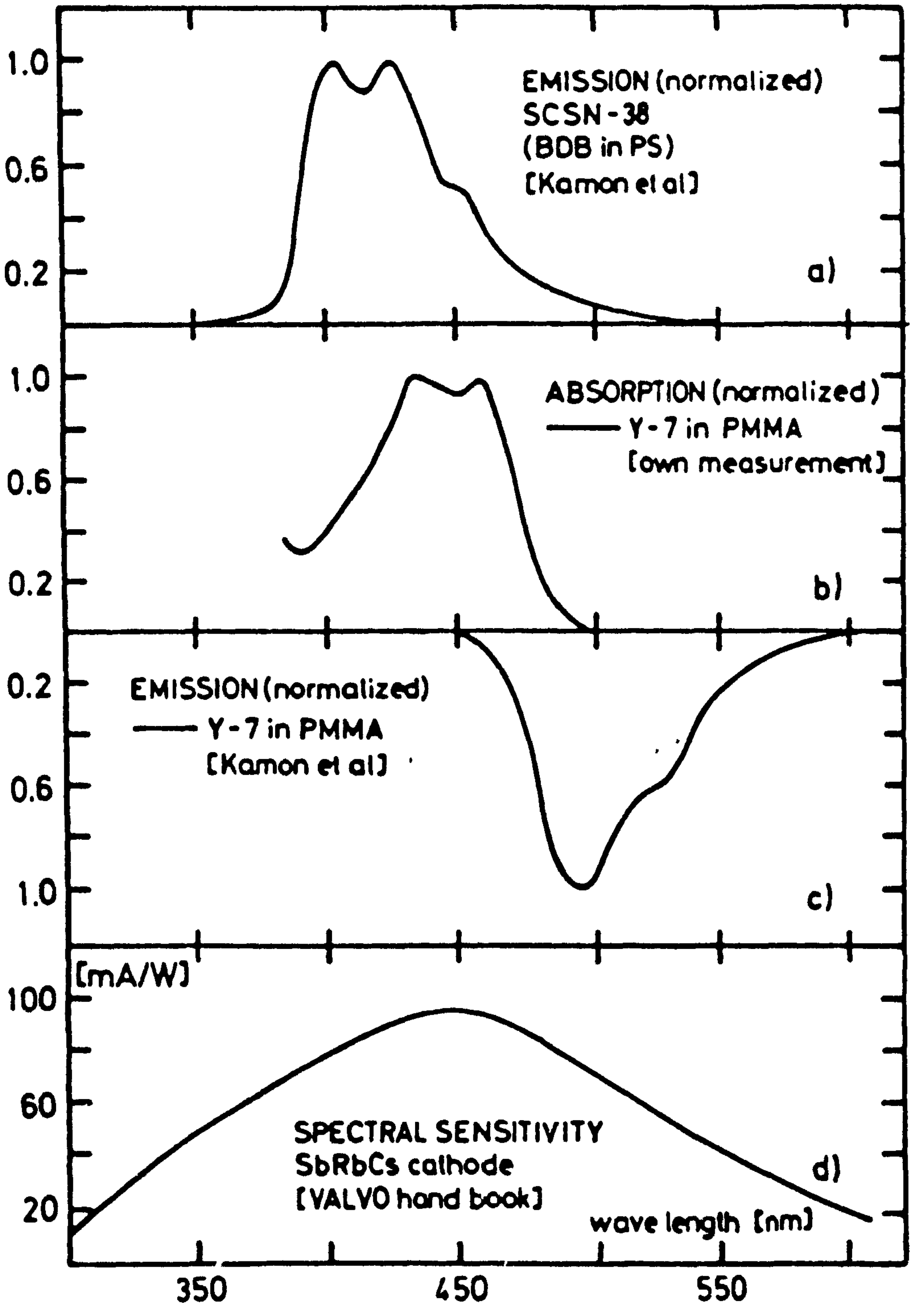

Figure 3.1: *Absorption and Emission Spectra of SCSN, Y-7, and PM cathode*

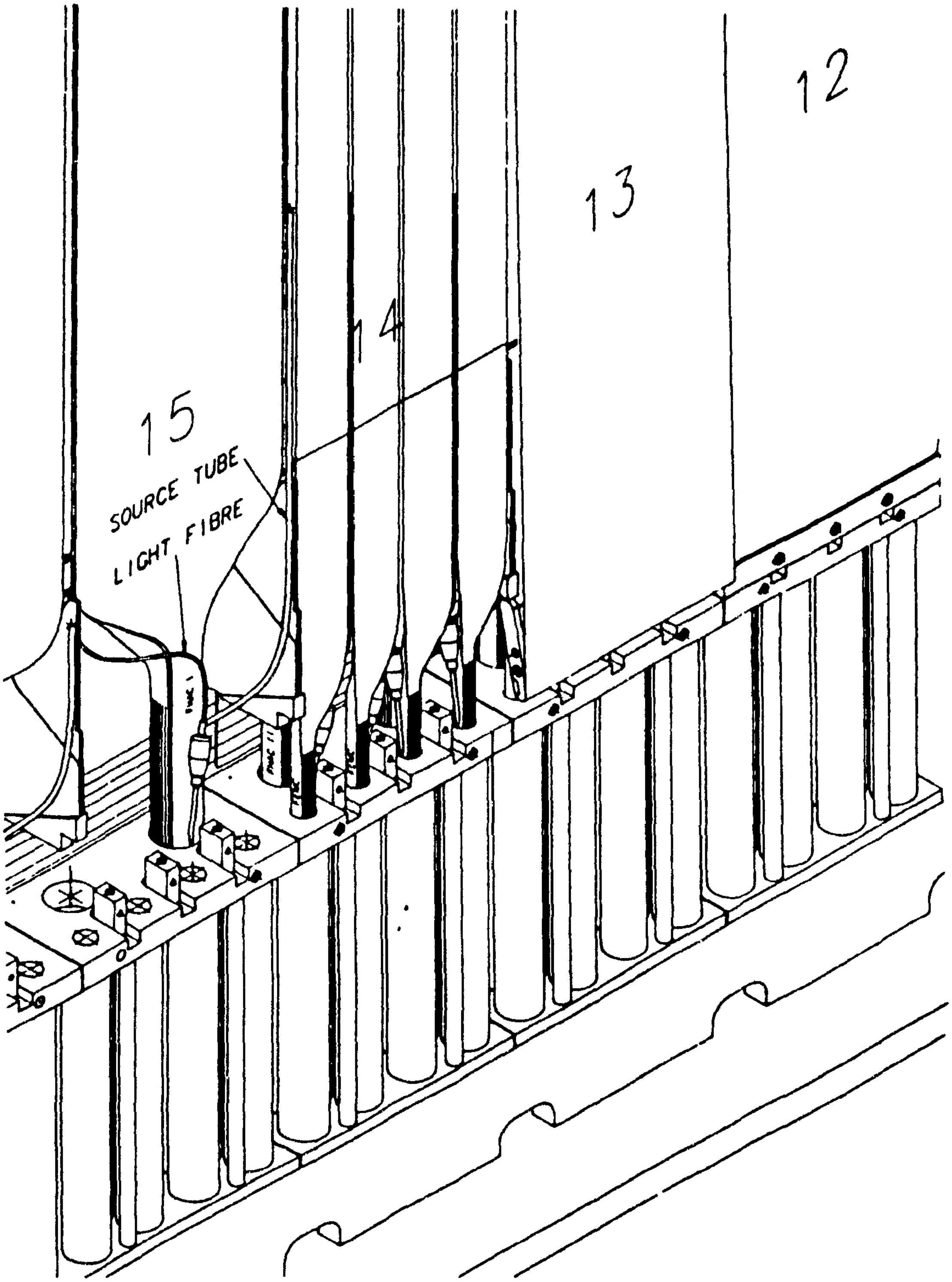

Figure 3.2: *View of the Source Guide Tubes and Light Guides*

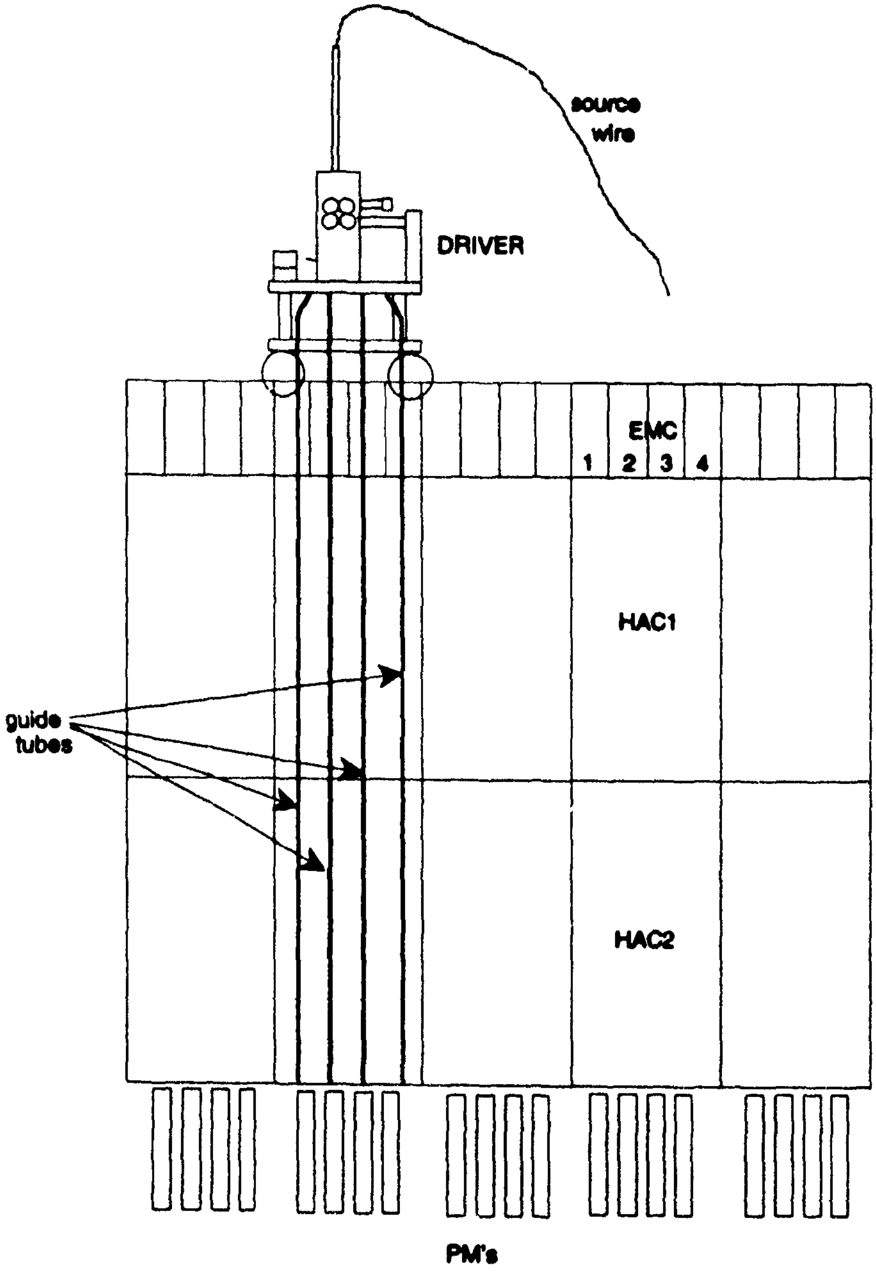

Figure 3.3: *Sketch of the outside driver scanning a module.*

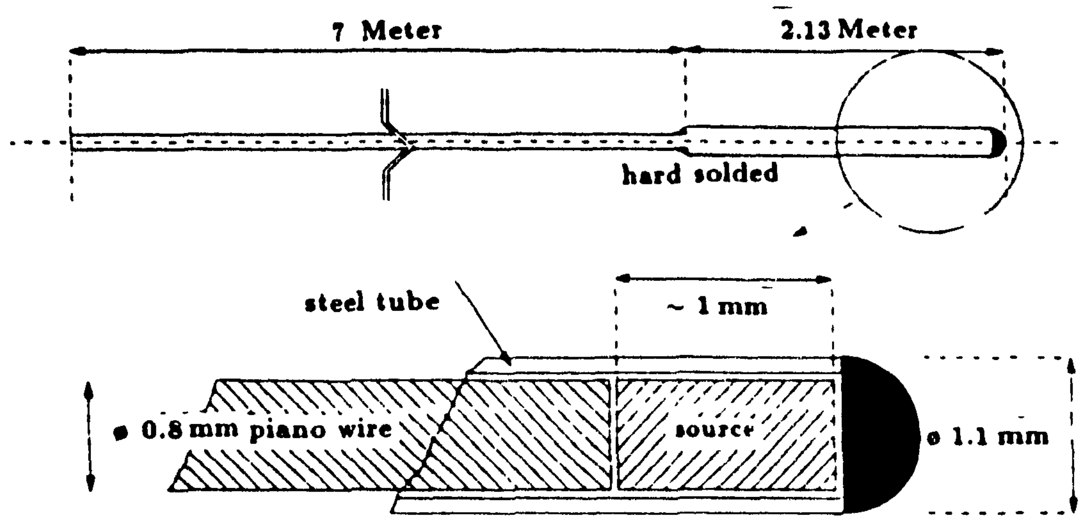

Figure 3.4: *Source wire used in inside scanning*

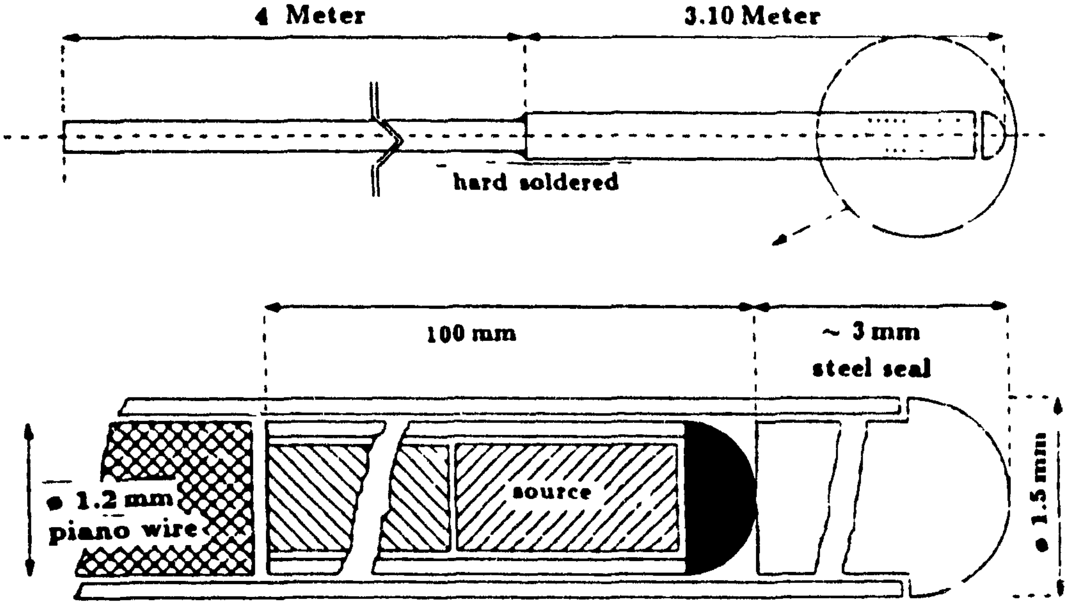

Figure 3.5: *Source wire used in outside scanning*

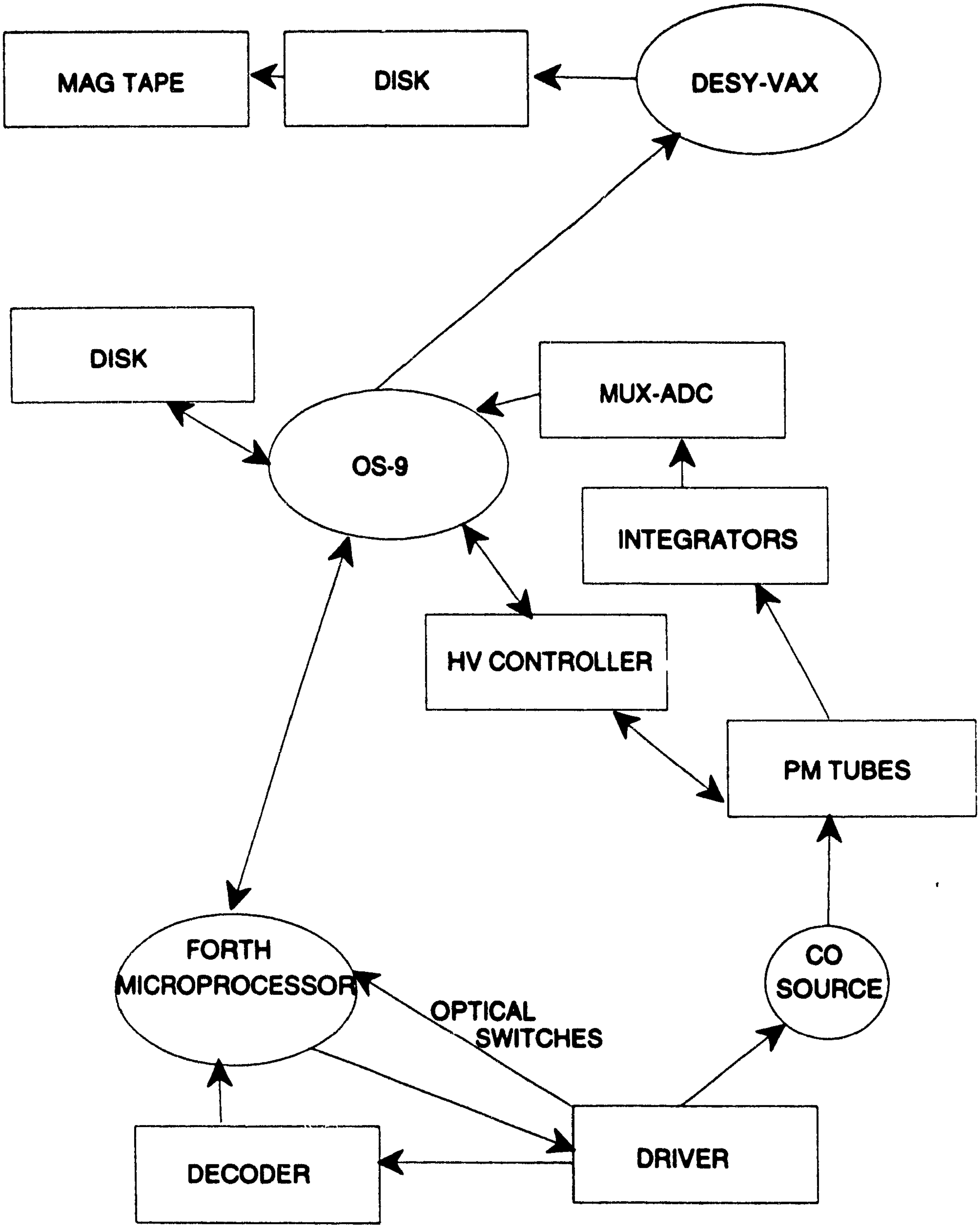

Figure 3.6: *Layout of Elements in the Run Control*

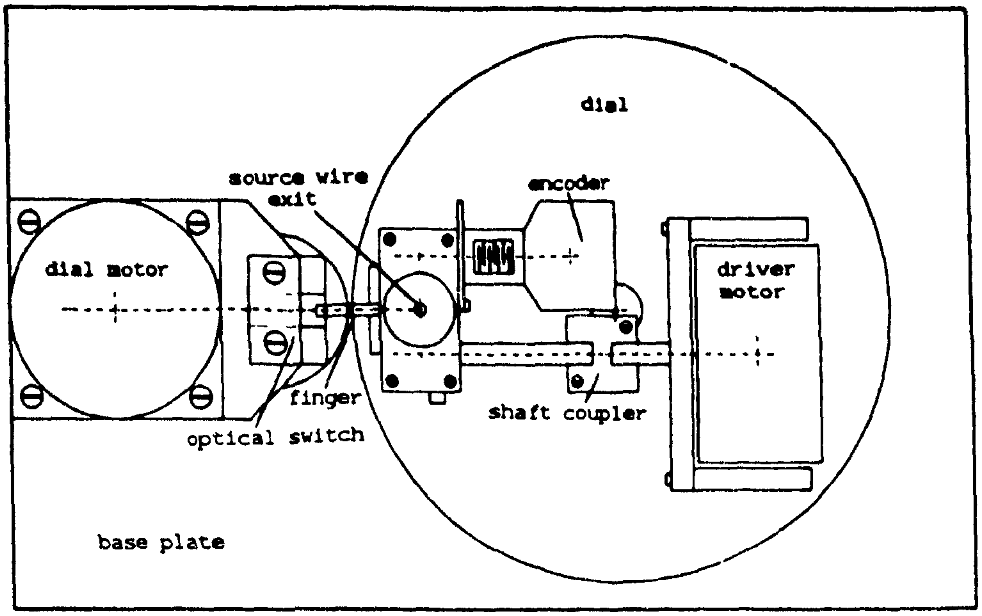

Figure 3.7: *View of Source Driver from above*

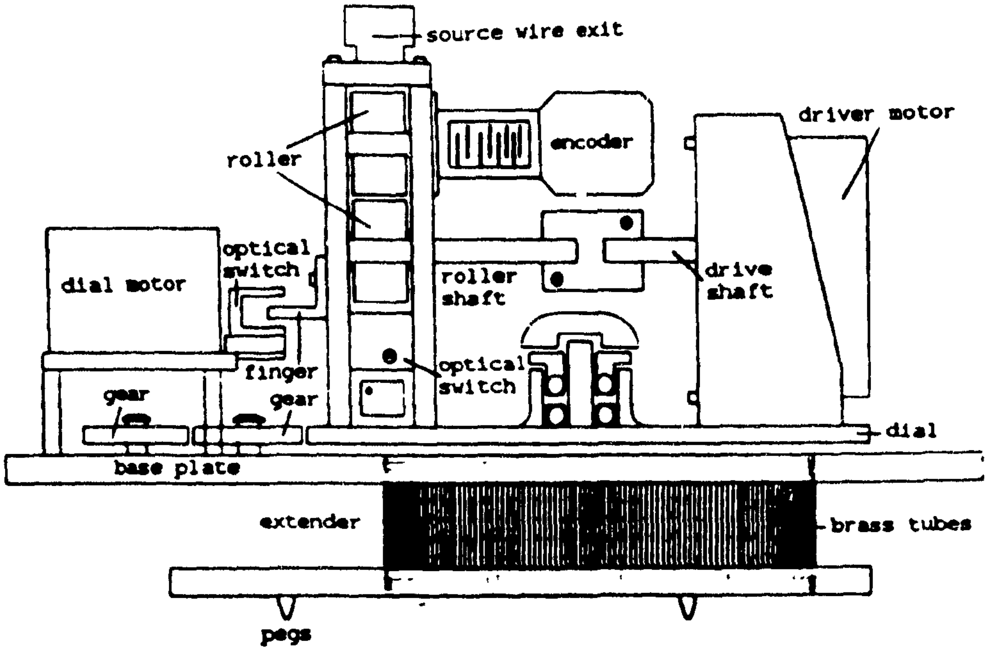

Figure 3.8: *View of Source Driver from the side*

Chapter 4

Monte Carlo

It is often helpful in understanding complex systems to simulate them with Monte Carlo programs. The actual processes involved may be individually relatively simple, but multiple consecutive interactions can quickly become exceedingly complicated and not analytically solvable. In our situation, the process of shower development is statistical in nature and lends itself naturally to Monte Carlo studies. The Monte Carlo program EGS4[28] was used to simulate the ^{60}Co scans. It is a successful program for simulating electromagnetic showers.

The user has only to define the detector's geometry and properties of its materials, specify the initial conditions of the input particle, choose the energy cutoffs and keep track of the energy deposition. Every region has an energy cutoff ECUT for electrons and PCUT for photons under which they will no longer be tracked. The particles are then assumed to deposit all their energy in that region. EGS4 (or its preprocessor PEGS) calculates the interaction cross sections for the materials. The user defines materials as compounds or mixtures of elements. For every material an AE and AP must be defined. AE and AP are respectively the energy cutoffs for electron and photon production in the material. Particles move in small steps, with each step bringing them either to an edge of a region or to the point of their next interaction. Also, for low energy electrons, a step size, which is the fraction of an electron's energy lost to ionization per step, can be set. This generally decreases the step distance for low energy electrons, increasing the accuracy of their tracks. Naturally the accuracy of the simulation improves with the lowering of the energy cuts. Unfortunately the computation time increases as well. Several different cuts were tried out and there did not seem more than a few percent difference between them. However the computation time varied significantly. The computation time was not significantly lengthened by using the lowest energy cut allowed for photons; 10 keV. Below this limit the approximations for the cross sections break down. The main drain of CPU time are the electrons, which move in small steps, depositing ionization energy and undergoing multiple scattering. The authors of the program recommend using a smaller than default step size when dealing with thin layers. In the end nonstandard cutoffs were used: ECUT = 1.0 MeV, PCUT = .01 MeV, AE = .711 MeV and AP = 01 MeV everywhere. A step size of 5% was used for steel and scintillator. The default step size was used in uranium, since it was assumed that most low energy electrons would not escape the uranium and penetrate through the steel foil surrounding it. For a million events it took about 5 hours CPU on a VAX 8600.

In the real ^{60}Co scans the data is taken roughly every .5 mm in the longitudinal direction, z. If we were to simulate the ^{60}Co scans in the same manner, i.e. by repositioning the source longitudinally along a tower, the amount of computer time required would be prohibitive. Instead, we can take advantage of the periodicity of the layer structure of a HAC section to find the signal response, $R(z)$, of a single scintillator as a function of the source distance in the longitudinal direction from the centre of the scintillator. We can then convolute the response from a single scintillator to get the signal from an entire section. A way to do this is to first define the geometry as having a large stack of DU/scintillator (in this case 120 layers) to avoid having to worry about edges. The number of layers is not important as long as the distance from the middle to the end is greater than the range of z in which we are interested. Next we run the Monte Carlo with the source along the stack at 8 different positions, spaced 0.5 mm apart in the z direction, starting at 0.25 mm from the centre of the middle scintillator (called the 0th layer, but actually the 60th of the 120 layers) of the stack to 3.75 mm from the centre. At the eighth position the source is actually opposite an uranium layer. If the source is at a distance z from the middle of the 0th layer, then it is a distance $8i - z$ from the middle of ith layer. This means that for a source sitting at position z, the energy deposited in the ith scintillator is $R(8i - z)$. If we also use the fact that $R(z) = R(-z)$ then the 0th scintillator gives data for 0.25 - 3.75 mm; the 1st scintillator covers 7.75 mm to 4.25 mm; the -1st scintillator is in the range 8.25 mm to 11.75 mm and so on. By combining the information from each scintillator layer we can construct $R(z)$ for any z. This function $R(z)$ obtained does have a slight correlation between points separated by a multiple of 4 mm because the values were generated by the same Monte Carlo run, but it should be removable by smoothing algorithms.

Once we have $R(z)$ we can find $S(z)$, the sum of the responses of eighty layers, by

$$S(z) = \sum_{i=0}^{79} c_i R(z - 8i),$$

where c_i is a measure of the efficiency of scintillator layer i and $z = 0$ mm is the location of the 0th scintillator.

A simplified but nevertheless detailed geometry of a HAC section was used. This is shown in Figure 4.1.

The tower was assumed to be large stack of DU/scintillator tiles. The ${}^{60}Co$ source was treated as a point source emitting 1.17 and 1.33 MeV photons with equal probability in a random direction in the hemisphere towards the tower stack. The source was placed outside the module as in an outside scan and 5 cm away in the lateral direction from the centre of the tower.

The raw shape of the source response is shown in Figure 4.2. The error bars are purely statistical and have no bearing on how well this shape matches the real results.

Actually, special measurements were done on several towers with the ${}^{60}Co$ source. In one such measurement, the strap was removed and the edges of all but one scintillator layer were covered. A ${}^{60}Co$ scan was then done normally. Figure 4.3 shows the real response of a single scintillator. The function obtained from the Monte Carlo

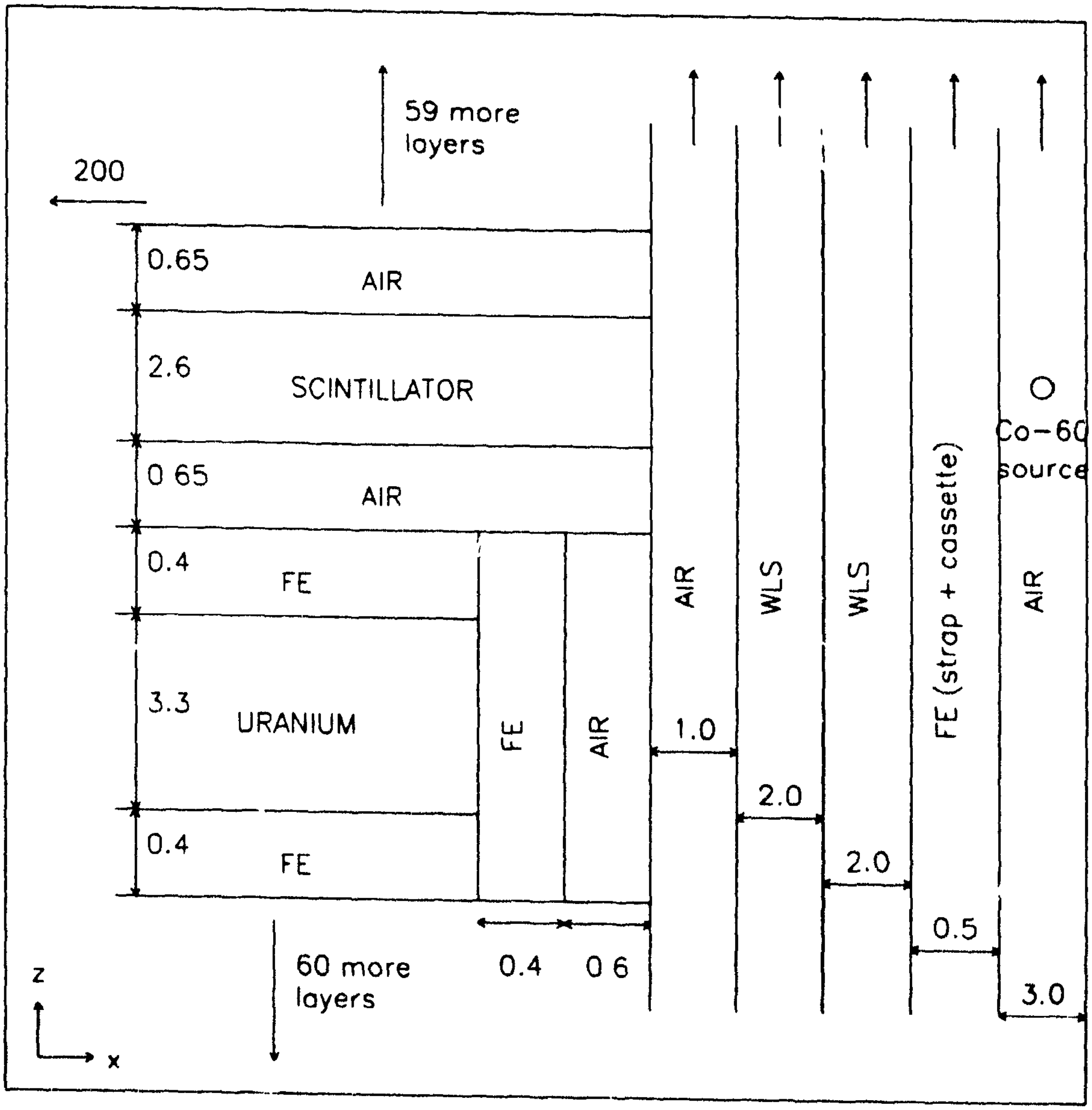

Figure 4.1: *Layer Structure used in Monte Carlo Simulation. Distances are in mm.*

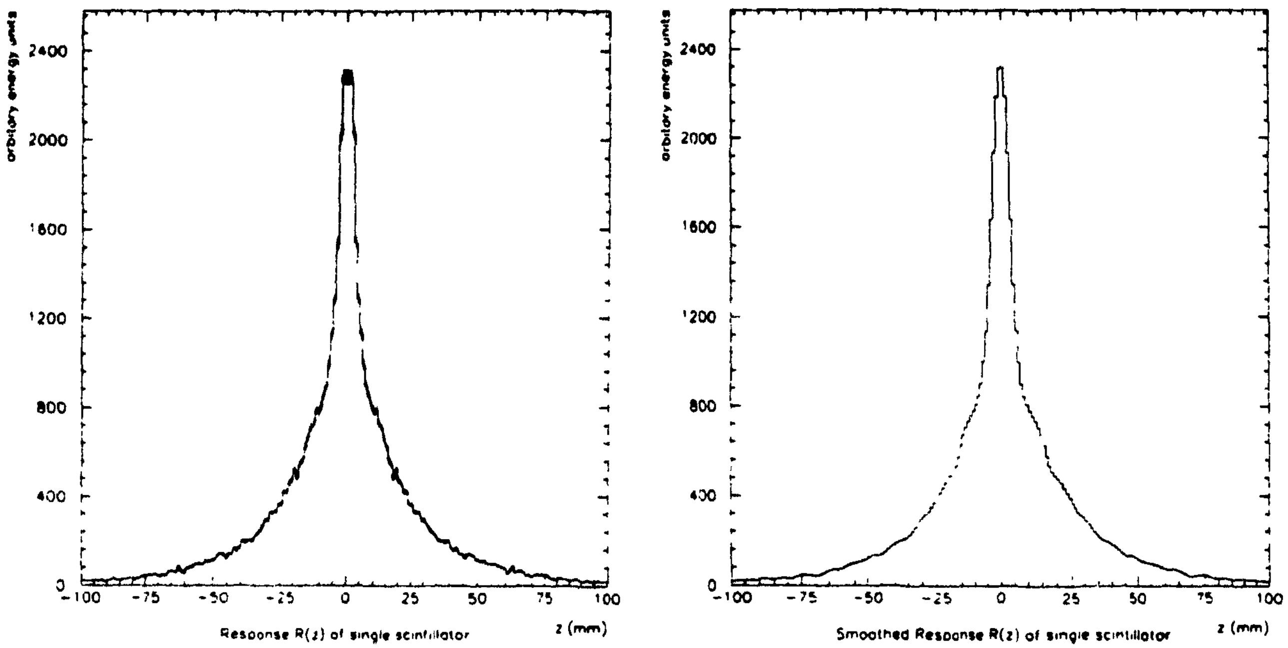

Figure 4.2: *Monte Carlo of the Response function, R(z), of a Single Scintillator, before and after smoothing*

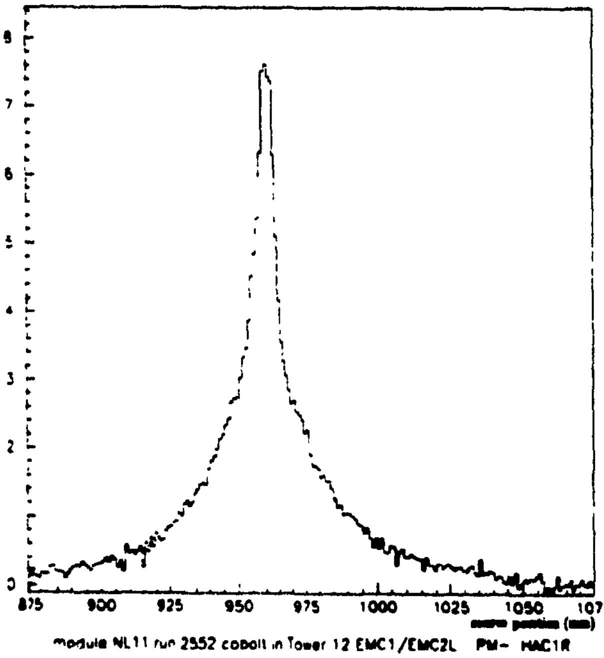

Figure 4.3: *Real Response of a Single Scintillator*

is slightly narrower than the real response but otherwise reproduces the shape fairly well.

After doing a 8 point filter on the raw shape from the Monte Carlo, and smoothing the distribution with the HBOOK routine HSMOOF we can apply the above formula to get the shape of a ^{60}Co scan from a 'good' HAC section (see Figure 4.4) The 8 point filter averages over the eight nearest points. The filtering and smoothing which decreases the correlation between points separated by 8 mm also significantly smooths the peaks and valleys representing scintillator and DU layers after convolution. This plot of the HAC section and the succeeding ones were in fact made by taking three Monte Carlo runs to find the response functions for scintillators projecting from the uranium by 0, 0.6 and 1.2 mm. Then in the convolution, 80% of the scintillators were assumed to be projecting out by the nominal distance of 0.6 mm The remaining 20% were assumed to be pushed in or out by another 0.6 mm and used the appropriate response function. The real scintillators are expected slightly shifted because of the cutouts in the scintillator for the spacers are slightly larger than the spacer size. This makes the shapes of the individual scintillator peaks seem less regular and more realistic. In addition, we assigned randomly to the coefficient c_i of $R_i(z)$ a value between .95 and 1.05 to reflect minor uncorrelated variances in scintillator thickness or WLS uniformity.

We can simulate what potential errors would look like by adjusting c_i to mimic the effects the errors would have on the the light output of the scintillators. For example, Figures 4.4 - 4.7 show plots with a 50% shadowed scintillator, bad stacking with some scintillators pushed out, bad stacking with some scintillators pushed in, and a linear dip in WLS response of 20% in the first 20 layers.

With the Monte Carlo we can investigate in detail some of the factors which affect the ^{60}Co scans which cannot be easily discovered experimentally. For example, the average depth where energy is deposited in the scintillator and consequently, where light is produced, is revealed through the Monte Carlo to be about 16 mm. Figure 4.9 shows the deposition of energy summed over all the scintillators in the x-y plane with

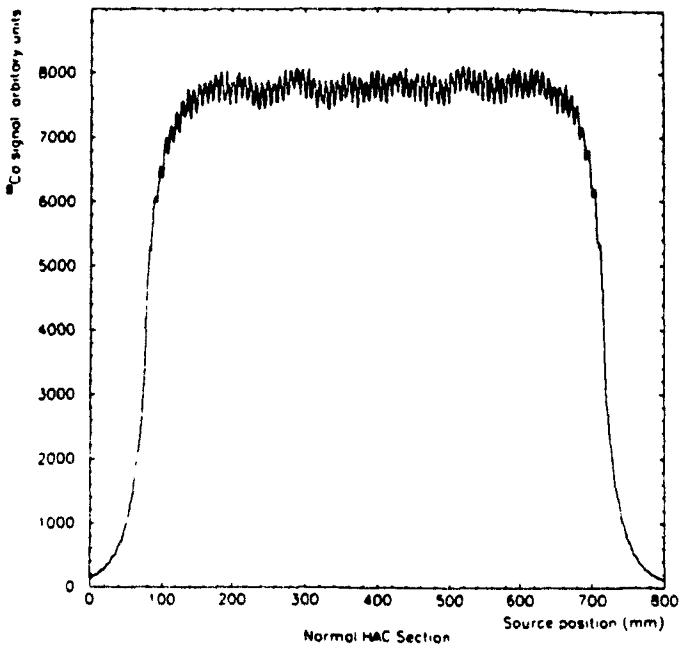

Figure 4.4: *Convoluted Response Function Representing Signal From HAC*

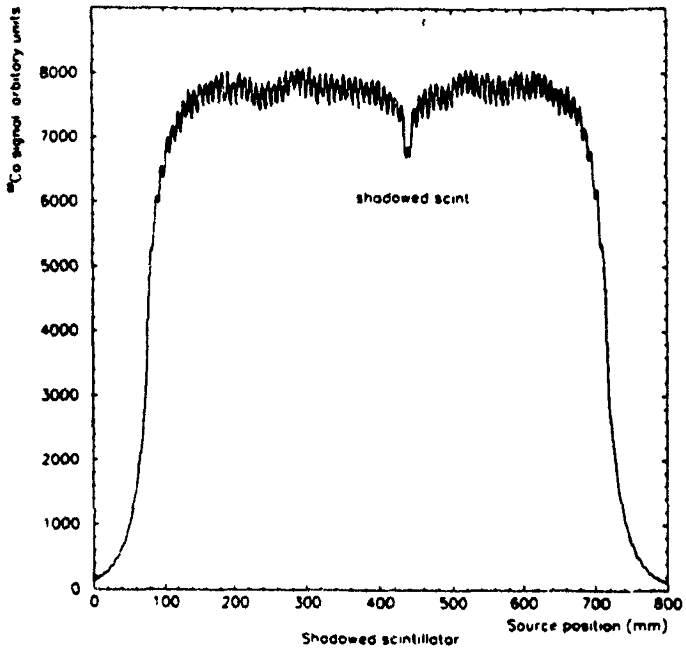

Figure 4.5: *Monte Carlo HAC section with one scintillator 50% shadowed*

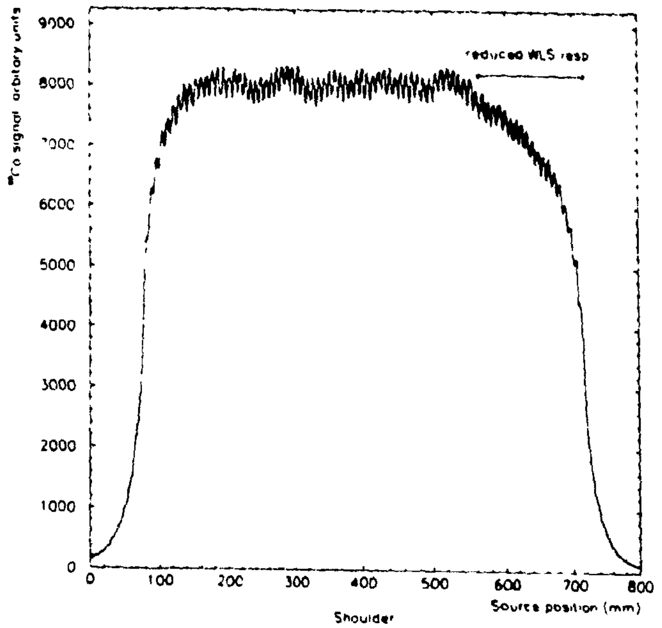

Figure 4.6: *Monte Carlo of HAC section with damaged WLS. The first 20 layers have a reduction in light output of 20% for the first layer, decreasing linearly to 0% for the twenty-first layer.*

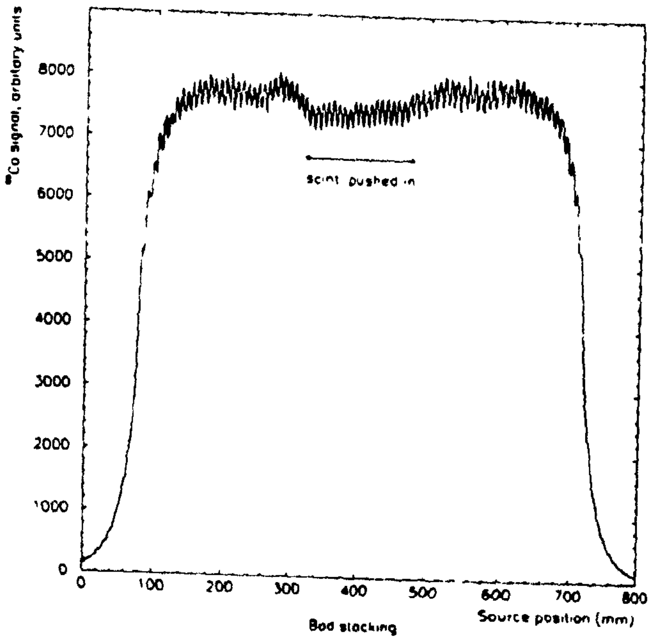

Figure 4.7: *Monte Carlo of HAC section with 20 layers pushed in by .6 mm*

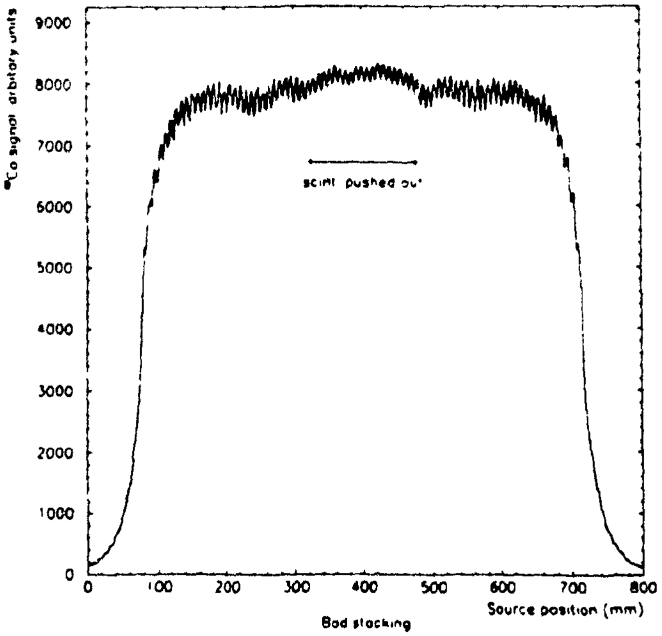

Figure 4.8: *Monte Carlo of HAC section with 20 layers pushed out .6 mm*

a ^{60}Co source at the origin. From the figure it is seen that not only does the ^{60}Co source have a limited penetration depth in the scintillators, it also illuminates only a small region along the edge of the scintillator. This implies that the ^{60}Co scanning can be very sensitive to edge effects and very local inhomogeneities which might not affect most particle showers because most showers are expected to occur away from the edges. Only part of a shower can occur in the edge regions because the cracks do not point towards the interaction region.

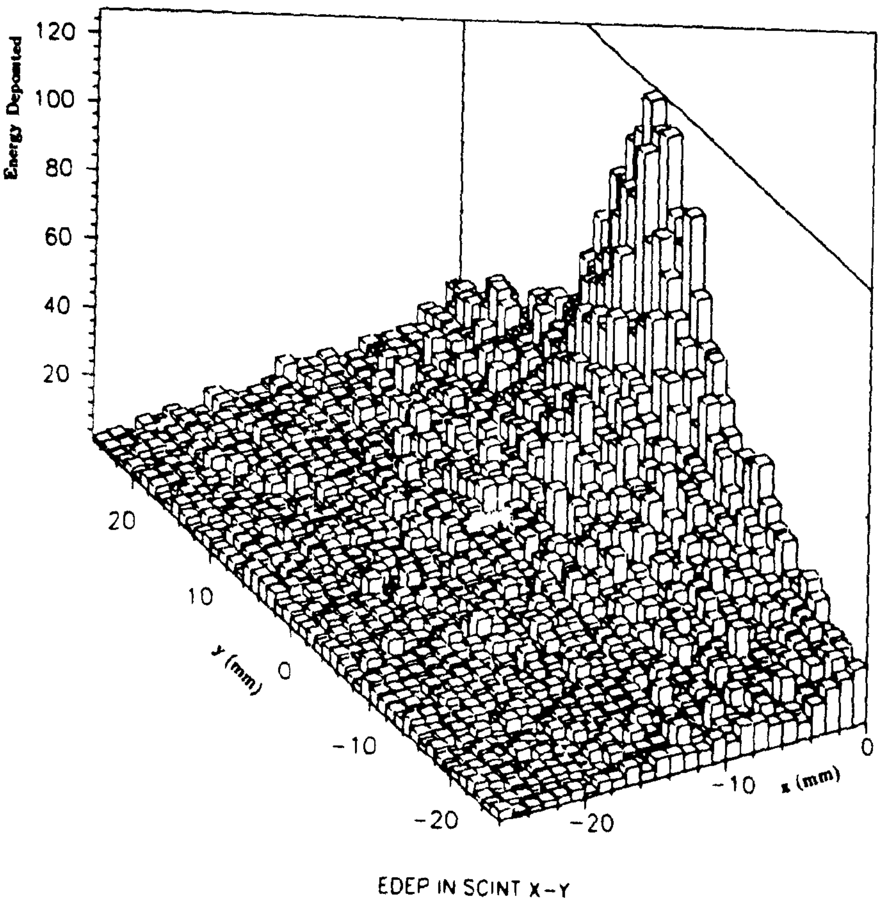

Figure 4.9: *X-Y distribution of energy deposited in scintillator with the source positioned at 8 mm away, as in outside scanning.*

Chapter 5

Results of ^{60}Co Scans

Before going into an analysis of the ^{60}Co scans the conventions used in describing a run should be defined. First, we distinguish between the two sides of a module by left and right, as defined from the perspective of someone sitting in the interaction region and facing the module. This also holds for the source driver. The guide tube labelled EMC1/EMC2 runs between EMC1 and EMC2 in FCAL and over EMC1 in RCAL. The tube labelled EMC3/EMC4 lies above the gap between the EMC3 and EMC4 WLS in FCAL and is over EMC2 in RCAL. The tubes used to scan the HAC0 towers are called either HAC01 or HAC02 and were positioned respectively on the lower or upper side of the tower.

5.1 ^{60}Co Signal

The signal from a calorimeter section undergoing a ^{60}Co scan can be divided into three parts:

- Uranium noise signal
- ^{60}Co signal from scintillator
- ^{60}Co signal from WLS (Cerenkov light)

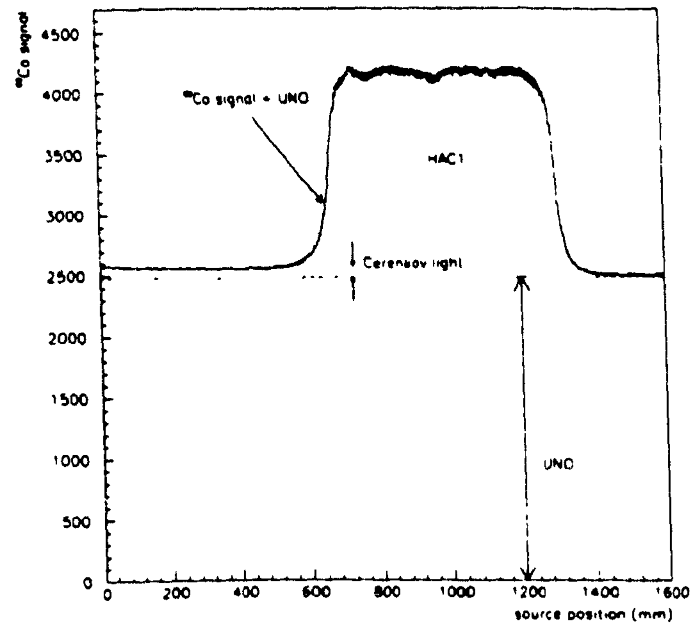

Figure 5.1: *Raw signal from PMs reading out both sides of a HAC section*

An activity of 2 mCi gives a ^{60}Co signal/UNO ratio during outside scanning of about 0.7 (0.5) in the HAC sections and 1.6 (1.2) in the EMC sections with the source on the same (opposite) side of the PM. The signal/UNO ratio for the inside scans were about 15% higher. The Cerenkov light is only seen when the source is on the same side of the PM tube being read out. In order to compare different towers we use, instead of the raw ^{60}Co signal, the signal/UNO ratio = (raw signal - UNO)/UNO. Sample plots of the signal/UNO ratio as a function of source position for normal sections are shown in Figures 5.2 - 5.5. These plots were all taken using the outside scanning procedure.

Each of the peaks corresponds to one scintillator. The little dips occur when the source is directly opposite an uranium plate. The EMC and HAC0 sections in FCAL (RCAL) have two (one) large valleys corresponding to the positions of the silicon gaps. The signal is reduced there because many of the gammas escape out the other end of the gap.

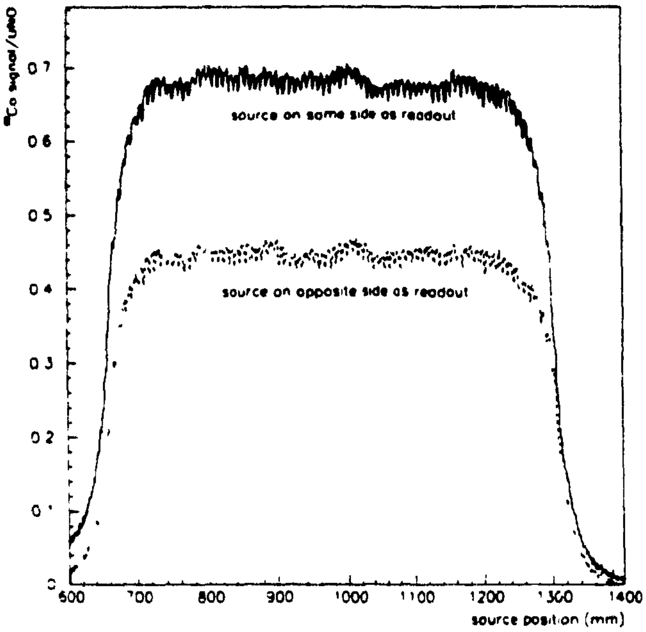

Figure 5.2: *Signals from PMs reading out both sides of a normal HAC section*

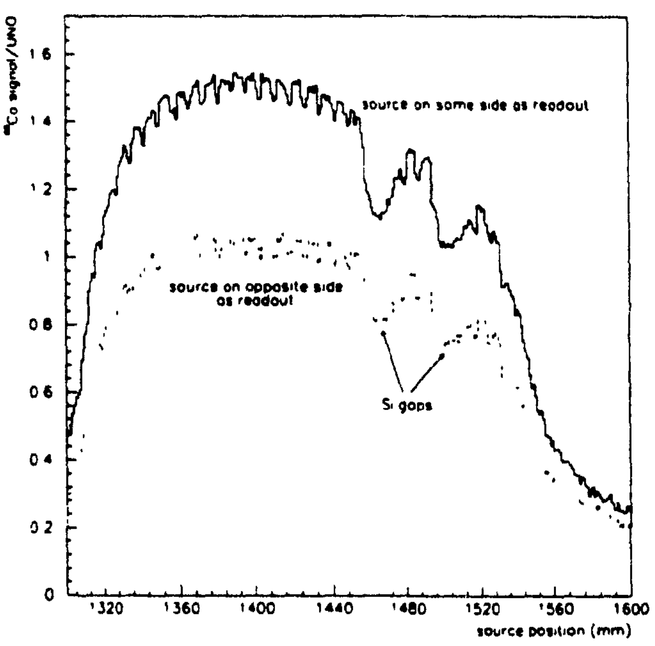

Figure 5.3: *Signals from PMs reading out both sides of a normal EMC section in FCAL*

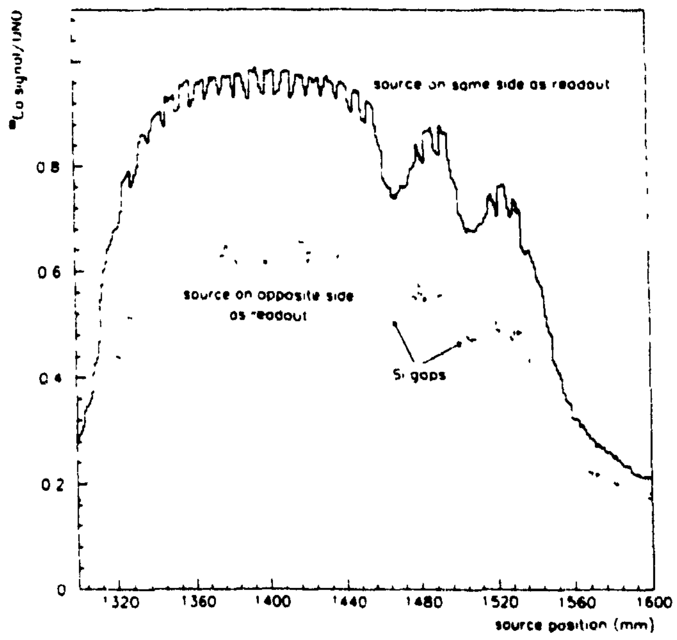

Figure 5.4: *Signals from PMs reading out both sides of a normal HAC0 section in FCAL*

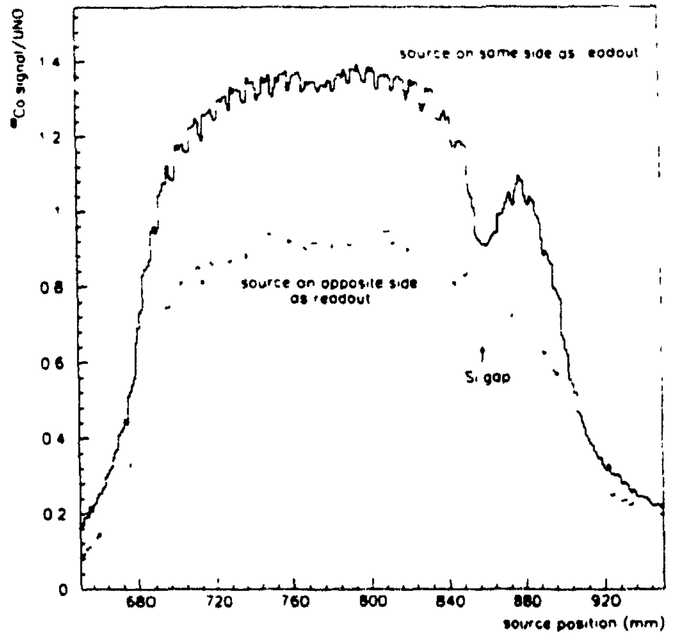

Figure 5.5: *Signals from PMs reading out both sides of a normal EMC in RCAL*

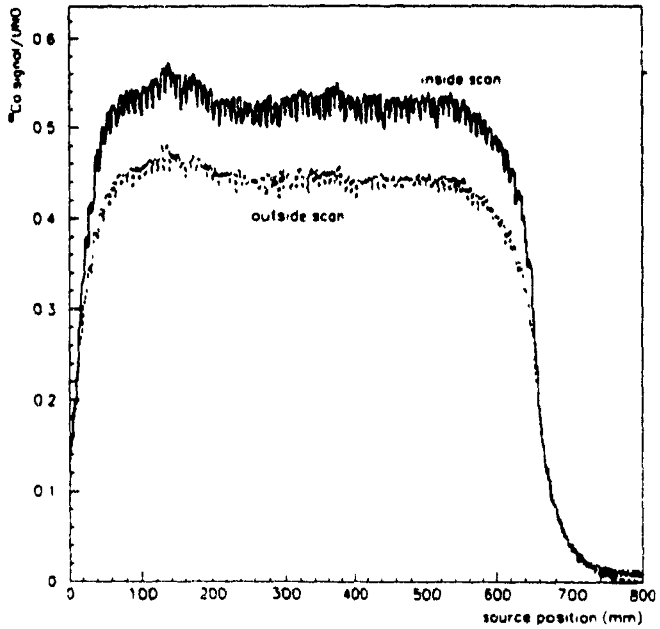

Figure 5.6: *Scans of Module CDN2, Tower 14 HAC2 with the inside and outside methods*

5.2 Reproducibility

Before trying to discover assembly faults from the analysis of the data from the ^{60}Co scans it should be shown that the results from the ^{60}Co scans are reliable and reproducible, to clear doubts on whether the inhomogeneities found are in fact caused by inhomogeneities inherent to the tower, or are mere artifacts from the scanning procedure. Figure 5.6 compares the results from the inside scanning and the outside scanning of a HAC section. Despite the decrease in signal in the outside scanning, it is clear that both methods reveal the same gross structure.

As test of the position accuracy of the source and its sensitivity to the the layer structure of the calorimeter we can determine the length of the sensitive layers of the HAC and EMC sections. This can be done by looking for the difference between the positions at which the gradient of the ^{60}Co signal is at a minimum or a maximum. Presumably this should occur when the source is just before the first or just behind the last scintillator. By comparing the results from inside scanning and outside scanning

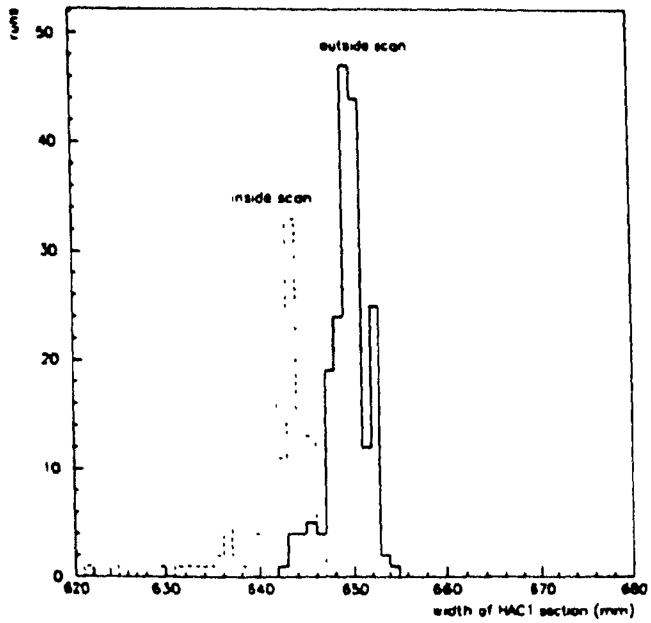

Figure 5.7: *Width of HAC1 sections from inside and outside scanning*

we can also clearly see in Figure 5.7 the difference the thicker source wire makes to the scale as discussed in Section 3 7.

The quality of the scans decreased somewhat in going from inside to outside scanning. The layer structure is still visible with outside scanning, but the scintillators at the borders of a section are less pronounced. The FCAL EMC sections were fairly sensitive to the precise location of the guide tube because the tubes run along the edge. The shape of the plot can be significantly distorted if the source runs over part of a neighbouring tile. This does, however, make the peaks more pronounced because the uranium acts as a collimator for the scintillator layer closest to the source. The price paid is a decreased signal/noise ratio and a greater sensitivity to small variations in the source position. The inside scanning tubes are placed exactly between the EMC WLS, whereas there were several millimetres leeway with the aluminum profiles used in the outside scanning. The inside guide tubes have the best of both· good resolution of the border scintillators and a well defined position providing a consistent shape of the scan data. All other scintillator tiles had the source tubes over the tiles, away from the edge, so this was not a problem for them.

5.3 Faults

All the modules were scanned by the outside method. The results from the scans were plotted and examined individually by eye. The ^{60}Co scans provide a visual impression of the quality of the section examined. Many types of potential faults can be characterized by correlated bumps and dips from different plots made with different source positions or readout sides. Recognizing faults was akin to pattern recognition, looking for relationships between the different scans. Naturally the human brain excels at such a task. The time to go through the plots of a module was a few hours, depending much on the experience of the examiner. During the scanning of a tower, the operator could in principle also go through the results of a previous module. Although computer programs[25][29] were developed to assist the analysis they were too undependable to cope alone with the wide variety of possible faults. They were used, however, to check the length of a section to see if a layer was 'missing'.

Faults are characterized by how the response varied with source position and on which side was the readout. In general, assembly faults occurring in the EMC section were of the greatest concern. Because the EMC section has only 26 layers, an affected scintillator therein contributes 4% of the signal, whereas in the HAC sections, a single scintillator comprises only 1% of the active volume. In addition, EM showers are almost totally contained within the EMC section As a consequence repairs were mostly done on the EMC sections and some faults in the HAC sections were left unrepaired due to a lack of time and manpower.

5.3.1 Bad Stacking

If the spacers were not properly positioned during stacking, the scintillators could end up shifted from their design position. This is quite noticeable when it occurs to a group of adjacent scintillators and is called bad stacking. The EMC2 and EMC3 tiles of FCAL were more prone to shift because they are not held in place by spacers. Sometimes the scintillator tile could be pushed back into place, but if the spacers

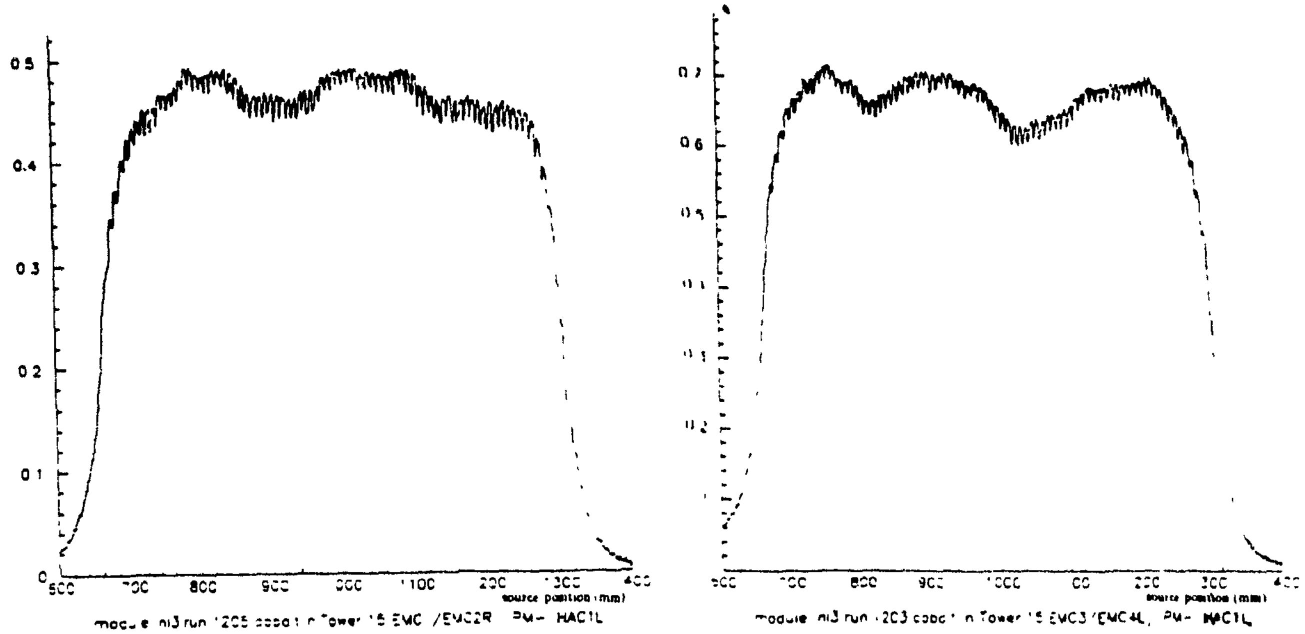

Figure 5.8: *Bad stacking*

were too far out of position, this could not be done. The bad stacking effects are seen by an increase (decrease) in signal in the region where the scintillators are pushed out (in) on the side where the source is. The change in signal is a result of the change of scintillator volume directly exposed to the ^{60}Co source. Figure 5.8 shows an example of bad stacking.

This is generally not considered to be a serious problem because the increased or decreased scintillator exposure is amplified by the source's position at the side of the stack. No effect should occur for small shifts (<0.5 mm) during a real shower where the particles are travelling transversely to the face of the scintillator unless they came straight down the edge of the stack. For larger scintillator shifts, it is possible that one end of scintillator will be shadowed by the uranium plate such that some of the light exiting the edge will be prevented from entering the WLS (see Figure 5.9).

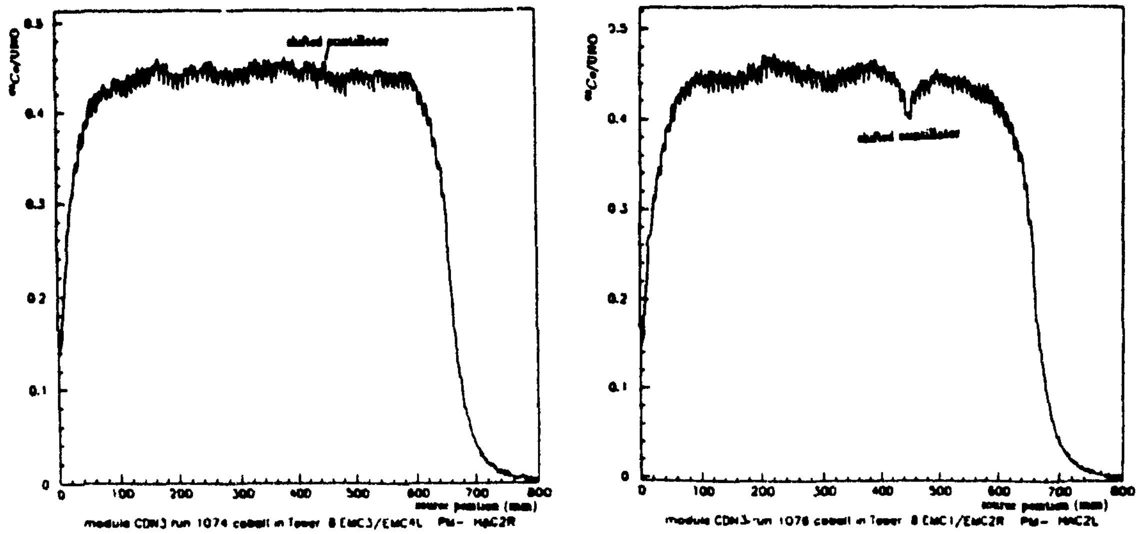

Figure 5.9: *Shifted Scintillator*

5.3.2 Bent WLS/Optical Contact

An interesting effect related to bad stacking occurred in module NL14. There the scans showed a significant increase in the response of the third scintillator on the right side independent of source position. Figure 5.10 shows the results of two scans, taken from the left and right sides. This effect was seen to varying degrees in over half the towers of NL14. Upon visual examination of the affected towers, three observations were noted. The third layer of scintillator had been shifted to the right. The nylon fishing line which normally separates the WLS and the scintillator edge had dug a groove into the edge of the scintillator. The WLS had a slight bend around the outcropping third scintillator, as it is constrained by the strap to fit against the edge of the front plate.

This suggests two possible explanations for the increased signal. One possibility is that the WLS and the projecting scintillator are in partial optical contact. This would allow light from the scintillator to enter the WLS directly, without any reflection from the surface. However, this might not be the correct explanation because optical

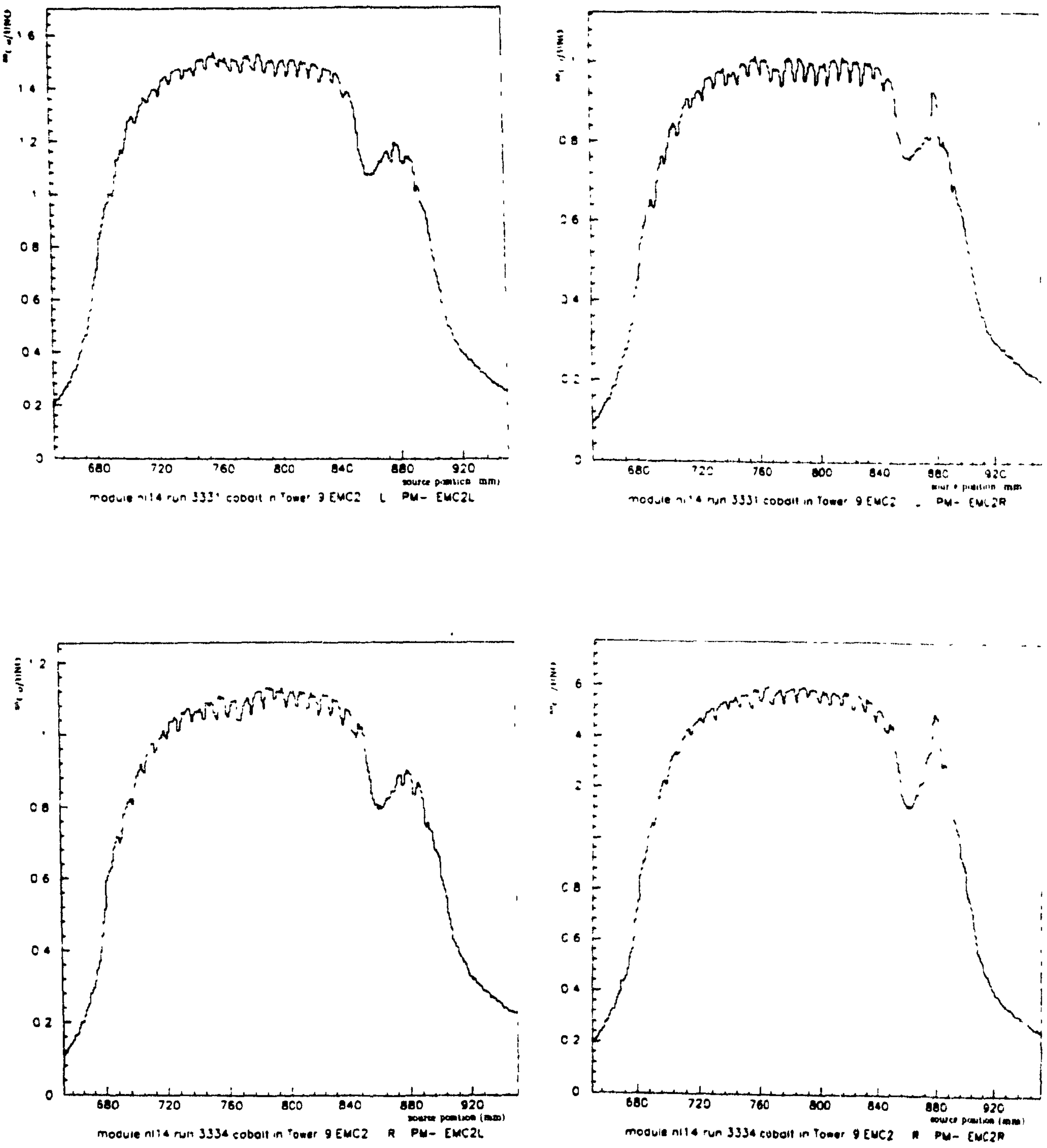

Figure 5.10: *Increased Response from Shifted Scintillator in NL14*

contact over a surface is difficult to achieve by pressure alone. The other suggestion advanced was that, because the WLS is bent around the third scintillator, light leaving the scintillator at sharp angles hits the WLS at an angle closer to the normal than usual. This would decrease the amount reflected off the surface and increase the light yield[30].

The reason this effect is not seen for other badly stacked scintillators further down in the stack is that the third scintillator juts out near where the WLS is forced to contact the front plate. This placed a lot of pressure in the region which would not have occurred further down the stack.

As it turned out, NL14 was one of the modules that went through beam testing at CERN. No increased signal response from the right side was seen. This is not surprising because the fraction of energy deposited in the third layer by a 15 GeV electron is not very different from the fraction that the layer contributes to UNO.

Whatever the cause may have been, the problem could not be fixed in the limited time and facilities available in the DESY preparation hall and the module was later installed without modifications.

5.3.3 WLS problems

Wavelength shifter problems should be detectable from ^{60}Co scans from both sides, and be seen in the signals from PM tubes on only one side. They were relatively easy to repair, requiring the removal and repair or replacement of the affected WLS cassette. This was done for all problems occurring in the EMC section and many in the HAC sections.

During the assembly of the WLS cassettes it was possible to put them together incorrectly such that after they were mounted, one or more sections would not be completely read out. It was also possible for cassettes to be incorrectly mounted such that the WLS for every section would not receive light from a scintillator layer (usually the first). For the EMC section, this would usually be quite visible from the scans (see Figure 5.11).

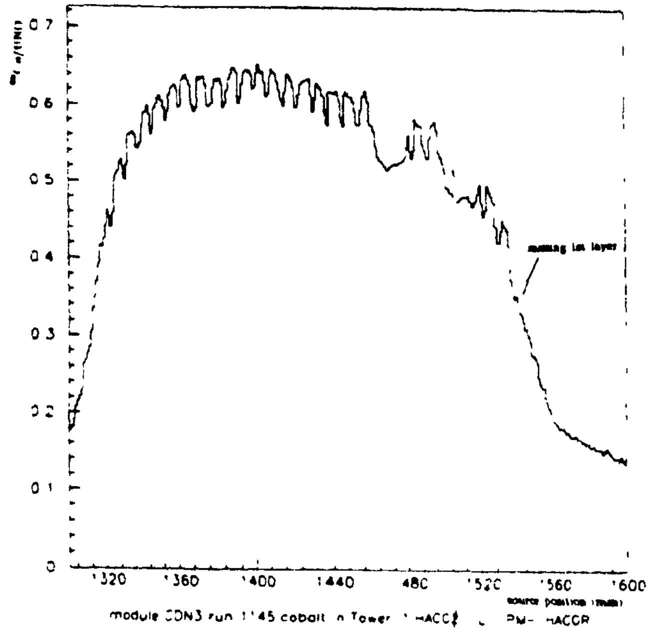

Figure 5.11: *Shifted EMC WLS. Note the sharp drop where the first scintillator layer should be indicating that the first layer is not seen*

Shifted WLS

For this reason it is important to know the width of the sections. If the width is 8 mm smaller than expected, then it is a clear indication of a shifted WLS. Similarly, the distance between the beginning and end of neighbouring sections can also be used to detect shifted wavelength shifters. Ideally, for example, the beginning of the HAC1 section as seen by ^{60}Co scans should also be where the EMC section ends. An alternative method attempted was to count the scintillator peaks. A fourier transform of the data was taken and the low and very high frequency components were removed. Since the peaks should occur every 8 mm, only the frequencies in this region were kept. After undoing the transform with the remaining frequencies, the signal remaining had very pronounced peaks corresponding to the scintillator positions. This made it easier to count automatically with a program[29].

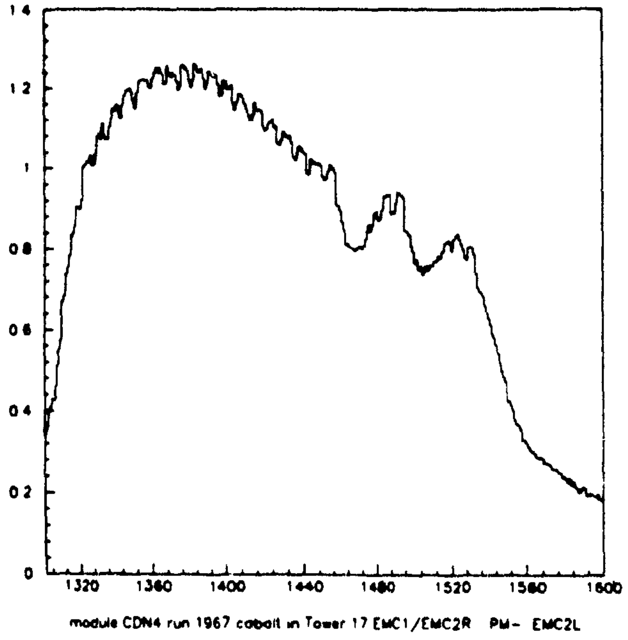

Figure 5.12: *Sticking back reflector*

Reflector Problems

Reflector problems range from a badly matching pattern which does not compensate enough to make the WLS uniform, to a sticking back reflector. Sticking back reflector problems could occur anywhere in the stack. The back reflectors are held in place at various points along the WLS. Occasionally they stick to it and total internal reflection is lost, reducing the light output. Figure 5.12 shows the result of a sticking back reflector occuring near the front of an EMC section. There is a steep drop in the response of the forward layers.

5.3.4 Light Path Obstructions

The presence of foreign material in the light path was easily detected and could easily be repaired by simply opening the tower and removing the offending piece of paper or plastic.

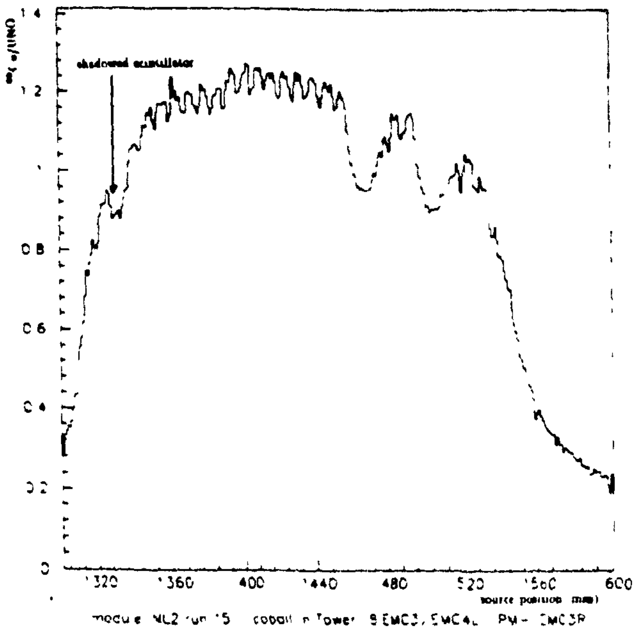

Figure 5.13: *Shadowed Scintillator*

Shadowed Scintillator

As it had been shown in the Monte Carlo results, the shadowing of a significant fraction of a scintillator tile in the middle of a stack is clearly visible. The black Tedlar sleeve was in some instances shifted over so that some of it went past the scintillator edge and folded over it. Figure 5.13 shows a scan revealing a depressed scintillator response.

Plastic Bags

In three instances sharp bumps were seen in one region of a section. One side would show an increased response over several layers independent of the source position. The other side had a depression in the same region, also independent of the source position. These towers were opened, and plastic bags were found where the bumps were. These clear plastic bags had been used in the packing of the WLS bars when they were shipped. They had been left on during the mounting of the WLS. The plastic reflected the scintillator light back into scintillator. This accounts for the increased response out the side opposite the bag. They were easily removed.

5.3.5 Inhomogeneities

By far the largest proportion of 'abnormal' ^{60}Co scans falls into the category of bad homogeneity These were generally characterized by bumps and dips which could not be explained after a visual inspection of the tower. Some of these bumps or dips occurred for a group of scintillators at one end of a stack. These were called steps. Others exhibited a slope in the plot over the entire section. These were called slopes. Slopes occurring at the edge of a HAC section were called shoulders. They did not seem to be caused by a WLS problem because both sides of the tower were affected.

For some, who have bumps and dips independent of source or WLS position, a logical connection is the composition of the scintillator themselves. For example, an effort had been made during the stacking to match scintillators from the same chemical batch within a tower. Perhaps for some towers, scintillator tiles from two batches, one of which with inferior optical qualities, were used, resulting in a step. Another possibility is a grouping of scintillators with a higher or lower thickness than average This would affect the volume of scintillator exposed to the source and change similarly manner the response. Figure 5.14 shows an example of a HAC section with large unexplained inhomogeneities.

Others had bumps and dips strongly visible only with the source on the side opposite the readout. This could be the result of faulty scintillators with a low attenuation length. Or it could be that the Tyvek paper somehow became damp and is stuck to the scintillator tile. This would destroy the total internal reflection and appear as a decrease in the attenuation length.

The frustrating part is that none of these hypotheses can be reliably verified without dismantling a module. This was not an available option, as the stacking machine was not present at DESY. Even had it been present, safety considerations and time limitations would not have allowed the dismantling of a module. This also makes it harder to estimate the effect of such a fault on a real shower.

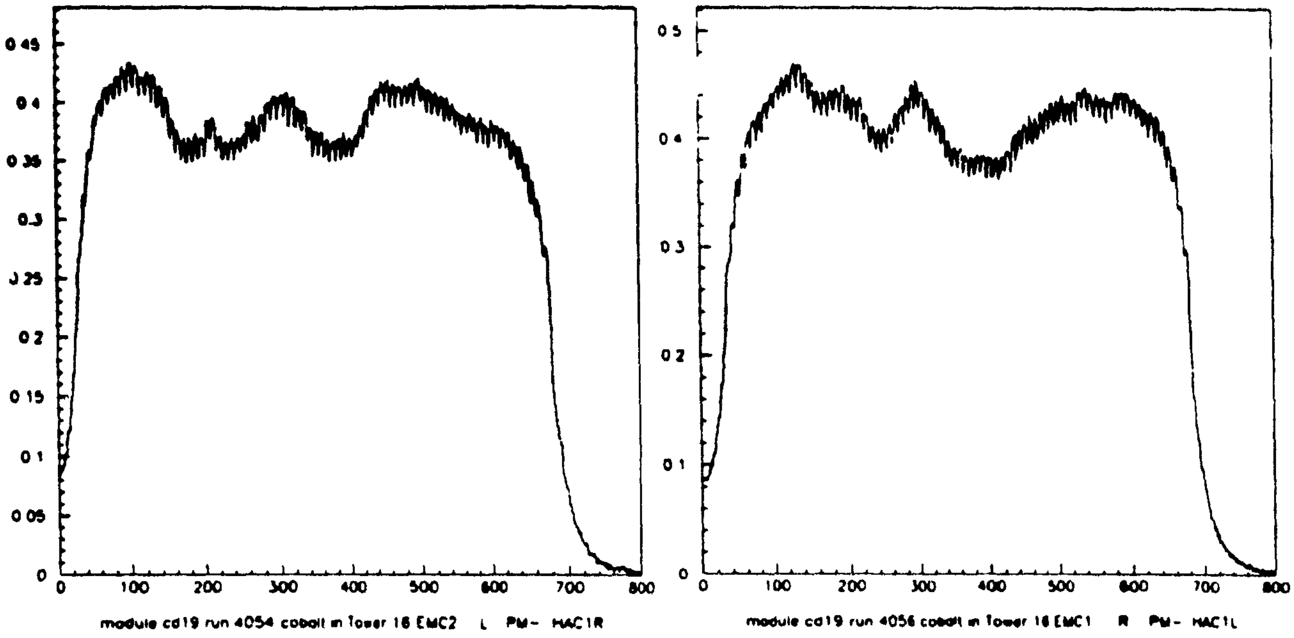

Figure 5.14: *Bad homogeneity*

5.4 Scintillator Attenuation Lengths

By comparing the signals taken by two runs from opposite sides of a tower a crude estimate of the scintillator attenuation length can be made[24]. We can use a simple model where the signal height is the product of the responses from the WLS and from the scintillator edge. The response from the scintillator is also attenuated. We take two runs, 1 and 2, taken from the left and right sides of the module respectively. The WLS response is W_R and W_L. S_R and S_L are the scintillator edge responses. d is the difference between the distances from the point of light production to the two edges.

$$E_{1R} = S_L \cdot W_R \cdot e^{-d/\lambda}$$

$$E_{1L} = S_L \cdot W_L$$

$$E_{2R} = S_R \cdot W_R$$

$$E_{2L} = S_R \cdot W_L \cdot e^{-d/\lambda}.$$

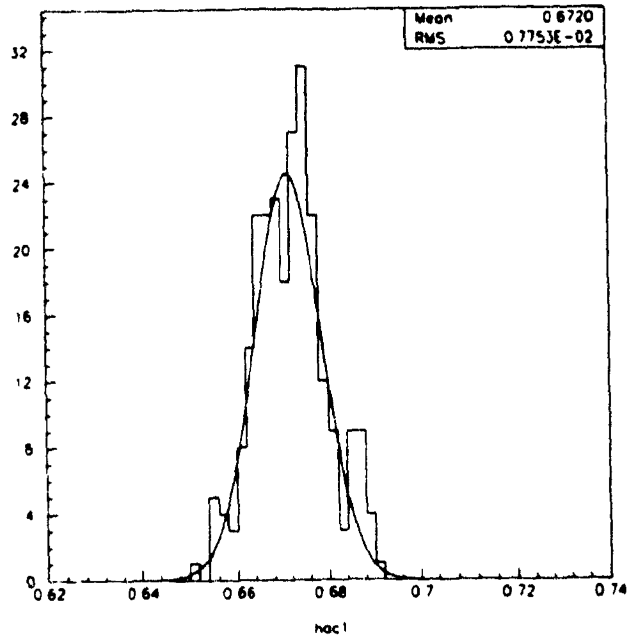

Figure 5.15: *Distribution of the quantity* $e^{-d/\lambda}$ *in FCAL HAC1 tiles*

Then the attenuation can be expressed as

$$e^{-d/\lambda} = \sqrt{\frac{E_{2L}E_{1R}}{E_{2R}E_{1L}}}$$

or

$$\lambda = -d/2\ln\frac{E_{2L}E_{1R}}{E_{2R}E_{1L}}.$$

Using $d = 16cm$ from the Monte Carlo, we get 40 cm as an average attenuation length for the FCAL HAC1 sections. As a comparison, beam tests conducted at CERN arrived at an attenuation length of about 70 cm [19].

The difference between the attenuation lengths calculated above and those obtained during test beam runs can be explained by edge effects. The scintillator light is produced very close to the edge. If there exists a gap between the Tedlar sleeve and the edge of the scintillator, it would be possible for light which would have normally been absorbed by the black sleeve to escape and enter the WLS. The second possibility is that light which would have been absorbed by one of the two fluors and then remitted isotropically goes instead directly out of the scintillator into the WLS.

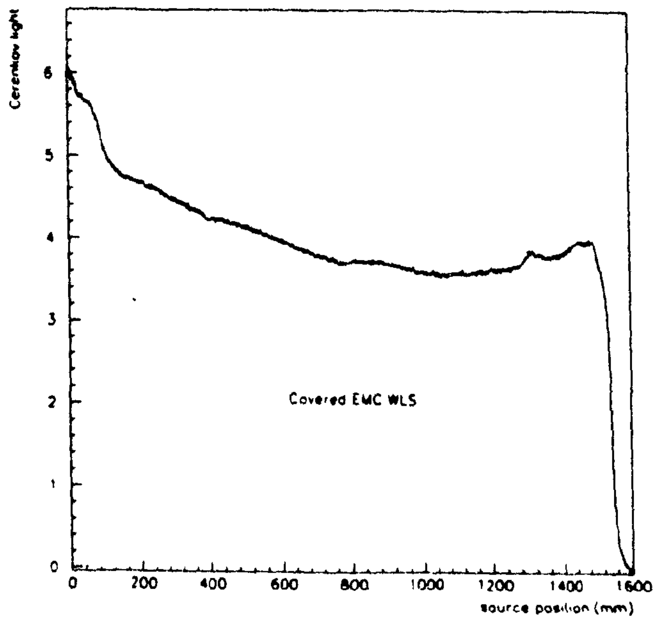

Figure 5.16: *Cerenkov light seen in a source scan with the scintillators covered*

The enhancement of signal from edge effects when the source is on the same side as the readout makes the attenuation length seem shorter.

Although the attenuation lengths calculated from the ^{60}Co scans are different from the beam test values, they can be used as a comparison with future ^{60}Co scans to monitor changes to the attenuation length. The narrowness of the distribution in Figure 5.15, of about 1%, gives encouragement that the changes of the same order can be detected in the future. A change of 1% in the value $e^{-d/\lambda}$ corresponds to a change of about 3% in λ.

5.5 WLS Attenuation

The attenuation length of the WLS can be determined by examining the amount of Cerenkov light emitted in the sections of the WLS not facing the scintillator[31]. In one of the special measurements a strap was removed and the edges of all the scintillators of a tower were covered. Only the Cerenkov light in the WLS reached the PM. Figure 5.16 shows the signal when the scan was taken. The gentle slope

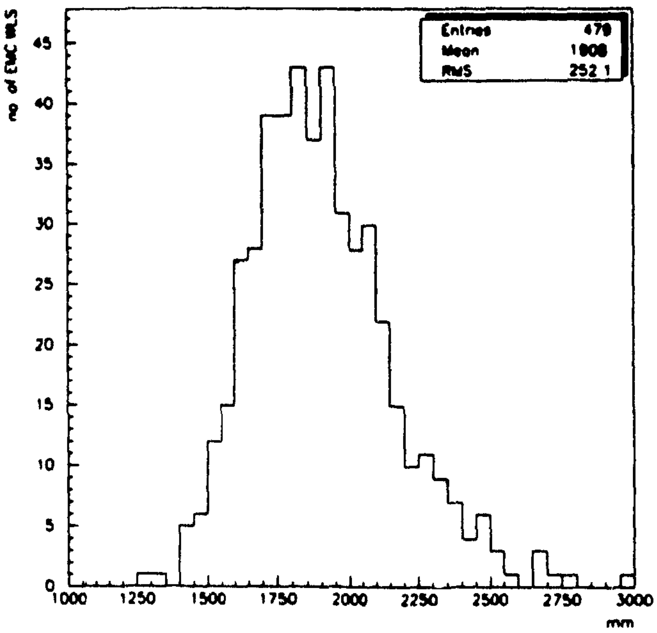

Figure 5.17: *Attenuation lengths of EMC WLS*

as the source moves away from the end of the WLS is due to the attenuation of the WLS.

This cannot be done after the modules are finally installed in the ZEUS detector. It is difficult to remove the contribution from the scintillators to the signal and leave only the Cerenkov light. Instead the regions where the WLS merely transports light and does not see scintillator light must be used.

For EMC WLS, this means fitting an exponential to the signal along the HAC sections. For the HAC1 section an exponential is fitted along the HAC2 section. The attenuation length of the HAC2 WLS cannot be measured in this way. The function fitted to the inactive regions is

$$I(x) = I_0(e^{-x/\lambda} + re^{(-x-L)/\lambda}),$$

where L is the length of the WLS; x is the distance to the to PM; r is the reflection coefficient of the end reflector. The distribution of attenuation lengths for FCAL EMC WLS is shown in Figure 5.17.

Chapter 6

Conclusions and Outlook

6.1 Scanning in the ZEUS Hall

Although the outside scanning method proved to be a reliable way to scan all the modules, it unfortunately cannot be used while the modules are installed in the ZEUS detector. Preparations are being made to improve the inside scanning method so it can be reliably used for at least a few modules. First, a new source is being prepared which will use a single long steel tube containing almost the entire length of the piano wire inside. This will avoid the bunching up of the wire which caused the friction problems with the earlier sources. Secondly, most of the brass guide tubes in RCAL plus those in the special half FCAL modules have been checked for badly glued joints with a dummy source wire pushed in by hand. 14 brass tubes had joints which opened during testing. In a further 66 brass tubes the end of the WLS cassette could not be reached. A few of the tubes were repaired. Most of the rest had their entrances closed. It is envisioned that a new outside scanner will be built which will run along the top C-arm of the special modules to scan the towers directly above the beam pipe in FCAL and RCAL while the clam shell is opened. Although only one side of the towers can be scanned in this way, it is hoped that enough information can be obtained to decide whether inside scanning is warranted.

6.2 Conclusions

^{60}Co source scans have been conducted from the inside for some and outside for all FCAL and RCAL modules. The source scans have proved to be very useful in detecting simple assembly faults. Most of the faults detected involving shadowed scintillators and faulty WLS have been corrected. Large inhomogeneities are often seen and have no confirmed cause, but are speculated to be connected with the scintillator uniformity. It is not clear what effects these inhomogeneities will have on the calorimeter's performance. A summary of the 'faults' can be found in Table 6.1 and Table 6.2. Although the cobalt scans cannot give the true attenuation lengths of the scintillators due to edge effects, it may be possible to monitor changes larger than a few percent to the attenuation lengths. The WLS attenuation lengths can also be reasonably monitored, though only for the regions receiving no direct scintillator light. A new and more mechanically reliable source is being prepared to continue inside scanning on the installed modules. Due to mechanical problems with the inside guide tubes, only selected towers are intended to be rescanned in the future.

Fault	Section		
	EMC/HAC0	HAC1	HAC2
Bad Stacking	3.0%	8.0%	6.5%
Shifted WLS	1.3%	7.6%	3.7%
Shadowed Scint.	0.5%	0.2%	0.9%
Bad Homogeneity *	0.5%	3.3%	0.4%
Shoulder *	-	1.1%	3.3%
Step *	0.1%	11.5%	9.1%
Slope *	-	2.8%	8.5%
Bump/Dip *	-	4.6%	6.1%

listing contains only faults ≥ 7%

* no satisfactory explanation yet found

measured towers: 460

of that 264 EMC towers

of that 196 HAC0 towers

Table 6.1: *Summary of Faults in FCAL*

Fault	Section	
	EMC/HAC0	HAC1
Bad Stacking	1.4%	5.8%
Shifted WLS	0.4%	1.1%
Shadowed Scint.	-	1.1%
Bad Homogeneity *	2.5%	13.3%
Shoulder *	2.1%	1.3%
Step *	4.7%	12.2%
Slope *	1.0%	12.2%
Bump/Dip *	2.0%	20.1%

listing contains only faults ≥ 7%

* no satisfactory explanation yet found

measured towers: 452

of that 256 EMC towers

of that 196 HAC0 towers

Table 6.2: *Summary of Faults in RCAL*

Bibliography

[1] M. Gell-Mann; A schematic model of Baryons and Mesons; Phys Lett. 8, (1964) 214-215

[2] E.D. Bloom et al.; High Energy Inelastic e-p Scattering at 6° and 10°; Phys. Rev. Lett. 23 (1969) 930

[3] G. Wolf; HERA: Physics, Machine and Experiments; DESY 86-089 (1986)

[4] Proceedings of the study of an ep facility for Europe; Ed. U. Amaldi; DESY 79/48 (1979) 391-394

[5] Proceedings of the HERA Workshop Vol. 1 and 2; Ed. R.D. Peccei; DESY (1988)

[6] ZEUS Collaboration; The ZEUS Detector, Status Report 1989 (1989)

[7] J.E. Brau and T.A. Gabriel; Nucl. Instr. and Meth. A238 (1985) 489

[8] R. Wigmans; On the Energy Resolution of Uranium and other Hadronic Calorimeters; Nucl. Instr. and Meth. A259 (1987) 389

[9] H. Brückmann et al.; Hadron Sampling Calorimetry, A Puzzle of Physics; Nucl. Instr. and Meth. A263 (1988) 136

[10] M.J. Berger and S.M. Seltzer; Tables of Energy Losses and Ranges of Electrons and Positrons; NASA-SP-3012 (1964)

[11] U. Amaldi; Fluctuations in Calorimetry Measurements; Phys. Scripta 23 (1989) 409

[12] Review of Particle Properties; Phys. Lett. 170B (1986) 45

[13] E. Ros; ZEUS-Note 86-135 (1986) (unpublished)

[14] R. Fernow; Introduction to experimental particle physics; Cambridge University Press (1986)

[15] M. Catanesi et al; Nucl. Instr. and Meth. A260 (1987) 43

[16] A. Sessoms et al.; The segmented calorimeter: A study of hadron shower structure, Nucl. Instr. and Meth. A195 (1982) 461

[17] H. Abramowicz et al.; Nucl. Instr. and Meth. 180 (1981) 429

[18] R. Klanner; Test Program for the ZEUS Calorimeter; DESY 87-058 (1987)

[19] ZEUS Calorimeter Group;Construction and Beam Test of the ZEUS Forward and Rear Calorimeter; to be published in N.I M.

[20] R. Blankers et al.; Construction of the ZEUS Forward/Rear Calorimeter Modules at NIKEF; NIKHEF-H 90-11 (unpublished)

[21] J. Straver; PhD Thesis; NIKHEF (1990)

[22] R. Garwin; The design of liquid scintillator cells, Rev. Sci. Instr. 23 (1952) 755

[23] I. Gialas et al.; Effect of light output nonuniformity on the ZEUS barrel calorimeter calibration; ZEUS-Note 89-109 (unpublished)

[24] U. Behrens et al.; First Measurements with Radioactive Sources in the FCAL Prototype Modules; ZEUS-Note 88-56 (unpublished)

[25] R. Krüger; Diplom Arbeit; Universität Hamburg (1990)

[26] D. Gilkinson; private communication

[27] R. Brun and J. Zoll; ZEBRA user guide, CERN program library entry Q100; CERN, Geneva (1987)

[28] W.R. Nelson, H. Hirayama, and D.W.O. Rogers; SLAC Report 165, Stanford: SLAC (1985)

[29] G. Gloth; Diplom Arbeit; Universität Hamburg (1991)

[30] G. Stairs; private communication

[31] F. Meyer; Diplom Arbeit; Universität Hamburg (1991)